



Article

Geospatial Modeling Based-Multi-Criteria Decision-Making for Flash Flood Susceptibility Zonation in an Arid Area

Mohamed Shawky and Quazi K. Hassan *

Department of Geomatics Engineering, University of Calgary, Calgary, AB T2N 1N4, Canada

* Correspondence: qhassan@ucalgary.ca

Abstract: Identifying areas susceptible to flash flood hazards is essential to mitigating their negative impacts, particularly in arid regions. For example, in southeastern Sinai, the Egyptian government seeks to develop its coastal areas along the Gulf of Aqaba to maximize its national economy while preserving sustainable development standards. The current study aims to map and predict flash flood prone areas utilizing a spatial analytic hierarchy process (AHP) that integrates GIS capabilities, remote sensing datasets, the NASA Giovanni web tool application, and principal component analysis (PCA). Nineteen flash flood triggering parameters were initially considered for developing the susceptibility model by conducting a detailed literature review and using our experiences in the flash flood studies. Next, the PCA algorithm was utilized to reduce the subjective nature of the researchers' judgments in selecting flash flood triggering factors. By reducing the dimensionality of the data, we eliminated ten explanatory variables, and only nine relatively less correlated factors were retained, which prevented the creation of an ill-structured model. Finally, the AHP method was utilized to determine the relative weights of the nine spatial factors based on their significance in triggering flash floods. The resulting weights were as follows: rainfall (RF = 0.310), slope (S = 0.221), drainage density (DD = 0.158), geology (G = 0.107), height above nearest drainage network (HAND = 0.074), landforms (LF = 0.051), Melton ruggedness number (MRN = 0.035), plan curvature (PnC = 0.022), and stream power index (SPI = 0.022). The current research proved that AHP, among the most dependable methods for multi-criteria decision-making (MCDM), can effectively classify the degree of flash flood risk in ungauged arid areas. The study found that 59.2% of the area assessed was at very low and low risk of a flash flood, 21% was at very high and high risk, and 19.8% was at moderate risk. Using the area under the receiver operating characteristic curve (AUC ROC) as a statistical evaluation metric, the GIS-based AHP model developed demonstrated excellent predictive accuracy, achieving a score of 91.6%.

Keywords: remote sensing; AHP; PCA; NASA Giovanni web tool; Sinai; Egypt



Citation: Shawky, M.; Hassan, Q.K. Geospatial Modeling Based-Multi-Criteria Decision-Making for Flash Flood Susceptibility Zonation in an Arid Area. *Remote Sens.* **2023**, *15*, 2561. <https://doi.org/10.3390/rs15102561>

Academic Editors: A. K. M. Azad Hossain and Taufique Mahmood

Received: 3 March 2023

Revised: 2 May 2023

Accepted: 11 May 2023

Published: 14 May 2023



Copyright: © 2023 by the authors. Licensee MDPI, Basel, Switzerland. This article is an open access article distributed under the terms and conditions of the Creative Commons Attribution (CC BY) license (<https://creativecommons.org/licenses/by/4.0/>).

1. Introduction

Flash floods occur when low-lying watersheds inundate rapidly [1], mainly due to short periods of extreme rainfall that exceed their water-holding capacity [2,3]. In addition to rainfall, other essential factors include (i) anthropogenic issues, such as unplanned development of flash flood prone areas [4]; (ii) hydrometeorological factors (e.g., temperature, evapotranspiration, runoff, porosity, and permeability); and (iii) geomorphic parameters, including the physical properties of watersheds [5]. However, the exact combination of processes and relevant factors that cause or regulate flash floods remains uncertain and unpredictable [6]. Moreover, unpredictable climate change amplifies the adverse effects of extreme precipitation events in warming seasons [7], causing severe recurrence of flash floods, especially in arid regions.

Flash floods are natural hazards that frequently occur worldwide, especially in arid Middle East regions such as Egypt. In fact, Egypt has recently experienced several severe flash floods, resulting in many life and property losses (<https://floodlist>).

[com/tag/egypt](https://floodlist.com/tag/egypt); accessed on 6 February 2023), with the following being notable examples: (i) The 12 November 2021 event in Southern Egypt (Aswan) resulted in the deaths of 3 people, the injury of hundreds from scorpion stings, and destruction to around 23 houses impacting at least 60 families, according to the initial governmental estimates (<https://floodlist.com/africa/egypt-aswan-floods-scorpions-november-2021>; accessed on 6 February 2023); (ii) the 13 March 2020 event in the governorates of Qena, New Valley, Sohag, and Menoufia claimed the lives of 5 people, caused 5 buildings to collapse, damaged drainage and water supply systems, and injured 13 people due to a train collision (<https://floodlist.com/africa/egypt-storm-floods-march-2020>; accessed on 6 February 2023); (iii) the 22–24 October 2019 event in the Gharbia, North Sinai, Kafr El-Sheikh, and Cairo governorates brought about the death of 8 people, flooded major streets, damaged airport infrastructure, and entailed flight delays (<https://floodlist.com/africa/egypt-cairo-floods-october-2019>; accessed on 6 February 2023); and (iv) the 26–28 October 2016 event in the lowlands across the governorates of Red Sea, Assuit, Qena, Sohag, and South Sinai led to the death of at least 22 people and injured 72 others, and resulted in the Egyptian government spending \$5.6 million in reconstruction efforts (<https://floodlist.com/africa/egypt-deadly-flash-floods-hit-sohag-red-sea>; accessed on 6 February 2023). Furthermore, recent climate changes manifest in extreme rainfall patterns and subsequent flash floods, particularly in arid regions such as Egypt [8,9]. Due to the problems mentioned above, it is critical to identify areas prone to flash floods to reduce their negative impacts on people, the economy, and the environment.

By analyzing present and historical dominant flash floods' causative factors (e.g., climatic, hydrologic, and geomorphic characteristics) in a specific location, it is possible to identify areas that are vulnerable to inundation (i.e., flash flood susceptibility modeling) [10]. Statistical, machine learning, and multi-criteria decision-making (MCDM) methods, or a combination of these approaches, can all be used to develop flash flood susceptibility models, which predict the likelihood and magnitude of future flash floods [11]. These models can categorize the hazard zones into distinct groups [12], and assess the geographic extent of past and future flash floods [10,13]. In addition, they can provide valued information for policymakers and governmental authorities to create emergency plans and mitigation strategies to reduce the loss of life and property.

Massive spatial datasets are mostly needed to monitor and model natural disasters but obtaining them might be difficult [14]. For example, in arid nations such as Egypt, field monitoring of rainfall and runoff datasets is often limited or absent [15], making it challenging and expensive to perform accurate spatiotemporal flash flood modeling using traditional observational methods [16]. Moreover, point-based field instruments recording rainfall and runoff can be time- and cost-intensive to collect vast and detailed geospatial data required to model natural hazards [17]. However, advances in remote sensing and GIS techniques have made it easier to monitor the spatial dynamics of flash floods (e.g., [18–23]). As an illustration, Earth observation-based satellites can repeatedly survey vast and inaccessible regions (e.g., mountainous and swampy areas) at a low or no cost. The geographic information system (GIS) also enables geospatial capture, storage, management, analysis, and presentations. In addition, it contains several cutting-edge algorithms, processes, and techniques that are valuable in flash flood monitoring and modeling applications (e.g., [5,24]).

Over the past years, several methods have been introduced for modeling flood susceptibility, including statistical approaches (e.g., frequency ratio [25] and weights-of-evidence [26]), as well as machine learning methods (e.g., artificial neural network (ANN) [27], decision tree (DT) [28], support vector machine (SVM) [26], and MaxEnt Entropy [29–31]). However, statistical approaches require testing a set of assumptions before initiating the study [32]. Moreover, machine learning techniques also have limitations when applied to flood susceptibility. ANN is a black box model that requires high computational capacity and extensive data for training and validation [33,34]. DT models are prone to errors caused by noisy data and do not allow for multiple output attributes [28]. SVM parameterization can be

time-consuming and requires many attempts for selecting the appropriate kernel type [35]. Finally, MaxEnt can be susceptible to overfitting the training datasets, leading to weak predictions (<https://pro.arcgis.com/en/pro-app/latest/tool-reference/spatial-statistics/how-presence-only-prediction-works.htm>; accessed on 6 April 2023).

The term “MCDM” refers to a set of tools and procedures for managing and ranking decision problems and alternative decisions [36]. One of the significant MCDM approaches that can efficiently model susceptible areas to flash floods (e.g., [37,38]) is the analytical hierarchy process (AHP) [39]. In the current study, the AHP was utilized to relatively weigh flash flood triggering factors and to generate a flash flood susceptibility index map. AHP is suggested by Saaty et al. [39] as an effective technique to support best decisions by setting alternative priorities that provide relative weights for multi-criteria problems using pairwise comparison matrices. Generally, the criteria weights and their alternatives are typically based on multiple experts’ subjective evaluations and personal experiences (e.g., [40,41]).

The AHP technique has been widely applied in various fields, including environmental planning, resource management, and hazard modeling (e.g., [41,42]). Some researchers have employed this method for modeling flash flood susceptibility in arid and semi-arid areas (e.g., [42–53]) (Table 1). In these studies, the priorities of flash flood triggering factors were initially assessed based on previous scholars’ judgments through detailed literature reviews or questionnaires via Google or email. A few studies employed the AHP technique to model and predict flash flood hazards in Egypt (Table 1). For example, Youssef and Hegab [38] selected the distance from the drainage network, slope, topographic wetness index, curvature, lithology, and elevation to identify areas prone to flash floods along the Ras Gharib area along the Red Sea coast. Other researchers applied the AHP model to detect flash floods hazards in the Biskra basin, Algeria [44], southeastern Tunisia [45], Shatt Al-Arab basin, Iraq–Iran transboundary [46], northeast of Tunisia [47], Taguenit, Morocco [48], Gabes basin, Tunisia [43], Dammam [49], Al-Qurayyat [50], Duhok, Kurdistan Region of Iraq [51], Wadi Al-Lith [52], Riyadh [53], and Najran [42] in the Kingdom of Saudi Arabia (Table 1). They commonly employed slope (S), rainfall (RF), elevation (E), drainage density (DD), distance from Wadis (DfW), land use/land cover (LULC), geology (G), and soil (So) as flash flood causative factors. Moreover, many of these models did not include a statistical multicollinearity test to identify correlated flash flood triggering factors, which may increase the inaccuracy in the developed flash flood susceptibility models (e.g., [42–53]). In addition, some of these studies did not include the key dynamic flash flood triggering factor (i.e., rainfall), such as Youssef and Hegab in Ras Gharib, Egypt [38], and Elkhrachy in Najran, Saudi Arabia [42] (Table 1). Furthermore, other researchers did not consider rainfall as the primary flash flood triggering factor, given that flash floods cannot occur without rainfall (e.g., [43–45,47–50,52]). It is worth noting that most of these studies did not employ statistical validation methods to evaluate the accuracy of their models’ predictions (e.g., [47,49,53]). Some researchers utilized pre- and post-optical satellite images such as Terra Moderate Resolution Imaging Spectroradiometer (MODIS)/surface reflectance MOD09GA [46], the Landsat TM 8 images-derived normalized difference water index (NDWI), and the normalized difference vegetation index (NDVI) to validate flash flood maps [43]. However, cloud coverage can limit the effectiveness of this approach [54].

Table 1. Literature review of the causative factors employed in AHP-based flash flood susceptibility modeling in arid and semi-arid areas.

Location/Authors	Factors Weights	Comments
Ras Gharib, Egypt Youssef and Hegab [38]	6 Factors: DfW (0.335), S (0.246), TWI (0.180), Cur (0.108), G (0.074), E (0.056).	Arid climate, no multicollinearity test, no rainfall, AUC = 83.3%.
Najran, Saudi Arabia Elkhrachy [42]	7 Factors: RO (0.355), So (0.240), S (0.159), SR (0.104), DD (0.068), DfW (0.045), LULC (0.030).	Arid climate, no multicollinearity test, no rainfall. For validation, the results were compared using two different DEMs for the study area.

Table 1. Cont.

Location/Authors	Factors Weights	Comments
Gabes Basin, Tunisia Dahri and Abida [43]	6 Factors: LULC (0.3298), G (0.1841), RF (0.1488), DD (0.147), S (0.1019), E (0.0883).	Semi-arid climate, no multicollinearity test. For validation, NDWI and NDVI extracted from Landsat TM 8 images (3 June 2014) were used to validate the flood map.
Biskra basin, Algeria Bouamrane et al. [44]	6 Factors: LULC (0.2775), So (0.217), RF (0.1599), DfW (0.1509), S (0.1478), E (0.0468).	Arid climate, no multicollinearity test, AUC = 93.61%.
Southeastern Tunisia Dhekra et al. [45]	8 Factors: E (0.225), LULC (0.175), G (0.175), RF (0.15), DN (0.1), DD (0.1), S (0.05), GWD (0.025).	Semi-arid climate, no multicollinearity test. For validation, the flood map was compared with the inventory map and evaluated using histograms of susceptibility zones.
Shatt Al-Arab basin, Iraq-Iran Allafta and Opp [46]	8 Factors: RF (0.1957), DfW (0.1606), E (0.142), S (0.1199), LULC (0.1107), DD (0.1057), So (0.0889), G (0.0565%).	Semi-arid climate, no multicollinearity test. For validation, visual verification using pre- and post-flood MOD09GA images was used.
North-East of Tunisia Hammami et al. [47]	8 Factors: LULC (0.23), E (0.18), G (0.18), RF (0.15), DD (0.10), S (0.08), So (0.05), GWD (0.03).	No multicollinearity and no statistical validation.
Taguenit, Morocco Ikirri et al. [48]	7 Factors: FA (2.73), DfW (2.54), DD (1.43), RF (0.71), LULC (0.85), S (0.55), P (0.40).	Arid climate, no multicollinearity test. Validation was carried out using fieldwork observations of the water level in 2018 and a survey of the local population.
Dammam, Saudi Arabia Dano [49]	5 Factors: RF (0.32), LULC (0.19), S (0.18), E (0.16), So (0.15).	Arid climate, no multicollinearity test, no statistical validation.
Al-Qurayyat, Saudi Arabia Abdelkarim et al. [50]	8 Factors: DfW (0.294), FA (0.190), S (0.190), RF (0.124), DD (0.082), RO (0.055), LULC (0.038), Hg (0.027).	Arid climate, no multicollinearity test, AUC = 97.1%.
Duhok, Kurdistan Region of Iraq Amen et al. [51]	12 Factors: E (0.207), S (0.174), DfW (0.174), RF (0.134), LULC (0.085), So (0.085), G (0.0378), TRI (0.037), TWI (0.0229), A (0.0174), STI (0.0116), SPI (0.0116).	Arid climate, no multicollinearity, the success rate for validation.
Wadi Al-Lith, Saudi Arabia Elsebaie et al. [52]	7 Factors: TWI (0.241), E (0.229), S (0.21), RF (0.103), DD (0.093), LULC (0.063), S (0.061).	Arid climate, no multicollinearity test. For validation, flood map was compared with the flood map of a 100-year return period.
Riyadh, Saudi Arabia Radwan et al. [53]	4 Factors: RF (0.54), S (0.24), DD (0.14), CN (0.08).	No multicollinearity and no statistical validation.

Abbreviations: Distance from Wadis (DfW), slope (S), topographic wetness index (TWI), curvature (Cur), geology (G), elevation (E), runoff speed (RO), soil (So), surface roughness (SR), drainage density (DD), landuse/landcover (LULC), rainfall (RF), drainage network (DN), groundwater depth (GWD), flow accumulation (FA), permeability (P), hydrological soil group (Hg), topographic ruggedness index (TRI), aspect (A), stream transport index (STI), stream power index (SPI), curve number (CN).

In response to the high occurrence of severe flash floods caused by global climate change, particularly in arid areas, the Egyptian government has implemented a sustainable development program for coastal regions to maximize its national economy. Previous studies on flash floods in southeastern Sinai were limited to geomorphometric analyses of the drainage networks (e.g., [5]). Integrating the AHP technique in the GIS environment proved to be a proper approach to modeling flash flood susceptibility. Incorporating expert judgments is essential in predicting areas prone to flash floods, but having multiple expert opinions can lead to a more subjective model. To address this issue, the current study employed the principal component analysis (PCA) algorithm to estimate the principal components that best describe the variation among the factors responsible for flash floods and reduce the ambiguity associated with personal judgments. In order to support future sustainable development plans, the current study's main aim was to identify and predict flash flood susceptible zones along the Gulf of Aqaba's coastal area in southwest Sinai,

Egypt. This aim was accomplished by employing available remote sensing datasets and improved PCA- and GIS-based MCMD techniques. The study had several objectives, which are as follows: (i) conducting a detailed literature review and drawing on the authors' previous experience to select 19 flash flood triggering factors; (ii) employing the Giovanni NASA web tool application to process the dynamic rainfall variable; (iii) implementing the PCA algorithm to identify variables that are relatively less correlated with each other; (iv) developing a GIS-based AHP model to identify areas susceptible to flash floods; and (v) evaluating the performance accuracy of the generated susceptibility map by comparing it with the flash flood inventory map.

2. Materials and Methods

2.1. Area of Study

The Sinai Peninsula occupies the northeastern part of Egypt with an area of 61,000 km². It has a triangular shape with an apex, where the Gulfs of Aqaba and Suez meet at the Ras Mohammed in the south [55]. The coastal zone of the Gulf of Aqaba is a crucial asset and has many investment opportunities, such as tourism, desalination plants, mineral exploration, and industrial zones. However, the rugged mountainous area alongside the Gulf of Aqaba's narrow coastal plain is susceptible to frequent destructive flash floods. These floods were mainly associated with incredible flow speed loaded by debris present, which threatened human life and infrastructure.

Flash floods are commonplace in the Middle East's arid areas such as the Sinai Peninsula [56]. Although Sinai generally has high evaporation potential, it is prone to extreme flash flood events because of the spatial heterogeneity of rainfall events with short duration and high intensity over a limited spatial extent [57]. Furthermore, many infrastructures (e.g., buildings and roads) are incorrectly located in the flash floods' paths [58,59]. Lack of attention has been given to flash floods in Sinai due to recording long intervals without extensive flash flood events. This unconsciousness gives residents a false safety message, thereby increasing their vulnerability to disastrous flood events.

The study area (Figure 1) covers approximately 1035 km² from south of the city of Dahab to north of the city of Sharm El-Sheikh along the southeastern coastal zone of the Gulf of Aqaba between longitudes 34°00' and 34°30'E and latitudes 28°00' and 28°30'N. The lithological setting of the study area is bounded from the west by basement badlands (i.e., igneous and metamorphic rocks), with a maximum altitude of 2279 m above the mean sea level. It slopes gradually and gently in the east direction to form the coalesced sedimentary alluvial plain along the western coast of the Gulf of Aqaba (Figure 1).

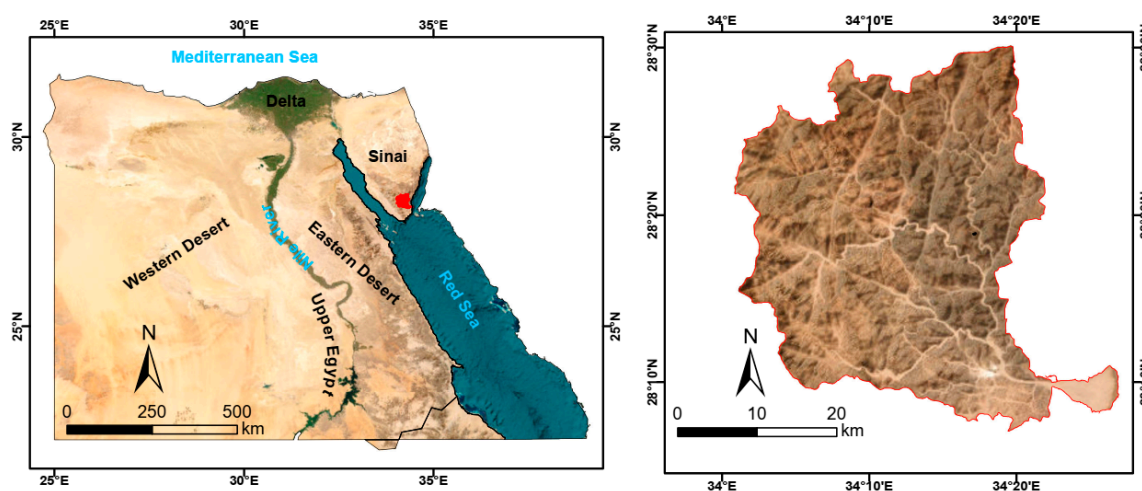


Figure 1. Wadi Kid, southeastern Sinai, Egypt. Service Layers Credits (Source): Esri, Maxar, Earthstar Geographics, and GIS User Community.

Wadi Kid is the largest area draining the study watershed area. However, limited studies (e.g., [5]) have been carried out to quantify the impact of flash floods on it. Though Wadi Kid remains dry most of the year, it transformed into an overflowing ephemeral stream after extensive rainfall events. Therefore, it supports vegetation growth due to surface and near-surface water availability. In addition, the area under scrutiny involves the Nabq area, declared by the Ministry of Environmental Affairs of Egypt as a multipurpose natural protectorate by Decree No. 1511 in 1992. It covers an area of 600 km², with arid climatic conditions dominated by a long, hot summer and a mild winter. It includes a unique combination of 134 plant species, migratory birds, coastal mangrove forests, and coral reefs.

2.2. Data

Ground data collection and monitoring during a disastrous flash flood is challenging, prohibitive, and sometimes impossible [38].

2.2.1. Flash Flood Inventory Map

A flash flood inventory map generally displays information on the date of occurrences, locations, and events that have left noticeable marks of their impact [38]. It was conventionally generated using fieldwork and aerial photographs of fine spatial details, but these traditional methods have limitations, as mentioned by Malamud et al. [60] and Guzzetti et al. [61]. Currently, remote sensing datasets are the primary source of information used to generate these maps, with minimal field surveys serving to verify the inventory maps [62]. Other authors use various sources to map the flash floods' inventories, such as in situ data collection, literature reviews, historical reports, satellite spatial images, and previously developed flash flood maps.

The current research generated the flash flood inventory map based on previous field data collection and developed a morphometric model for detecting flash flood-prone areas described in Taha et al. [5]. In addition, this inventory map was visually verified using the previous literature, Google Earth Pro, and volunteered geographic information. Despite the unscientific nature of volunteered geographic information (e.g., information from sources such as the internet, media, newspapers, and local settlers), they can introduce crucial information for natural hazards studies [63]. Furthermore, integrating this type of information with conventional data introduces valuable information for mapping the flash flood extent. Therefore, some researchers have effectively used volunteered datasets to help detect flash flood inundation [64–70]. Non-flood points were mainly collected by using Google Earth Pro and generally restricted to the upstream area (i.e., elevated rugged hills and mountains that are not impacted by the flash flood events) (e.g., [12,71,72]). Figure 2 shows randomly selected flood ($n = 100$) and non-flood ($n = 100$) points extracted from the flash flood total inventory map of Wadi Kid across the drainage network of southeastern Sinai, Egypt.

2.2.2. Description of the Digital Elevation Model (DEM) Used in the Current Study

Many flash flood causative factors can be directly or indirectly extracted from the digital elevation model (DEM). DEM is commonly used to demonstrate digital elevation datasets and present the terrain landscape relief of a given terrain, where the altitude values are represented as a regular array of Z values, which are georeferenced to a common world datum [73]. The freely available global ALOS Phased Array type L-band Synthetic Aperture Radar (PALSAR) DEM with an original spatial resolution of 12.5 m was employed in our current study to extract different spatial layers due to its high horizontal and vertical accuracy (i.e., 4.57 m) [74]. The PALSAR DEM was initially developed and processed by the Alaska Satellite Facility Distributed Active Archive Data Center (ASF DAAC). The internal side-looking of SAR images was corrected using Gamma software to enhance the backscattering signals' estimation and reduce the foreshortening and layover (i.e., geometric

distortion). For more information on PALSAR DEM generation and characteristics, refer to Laurencelle et al. [75].

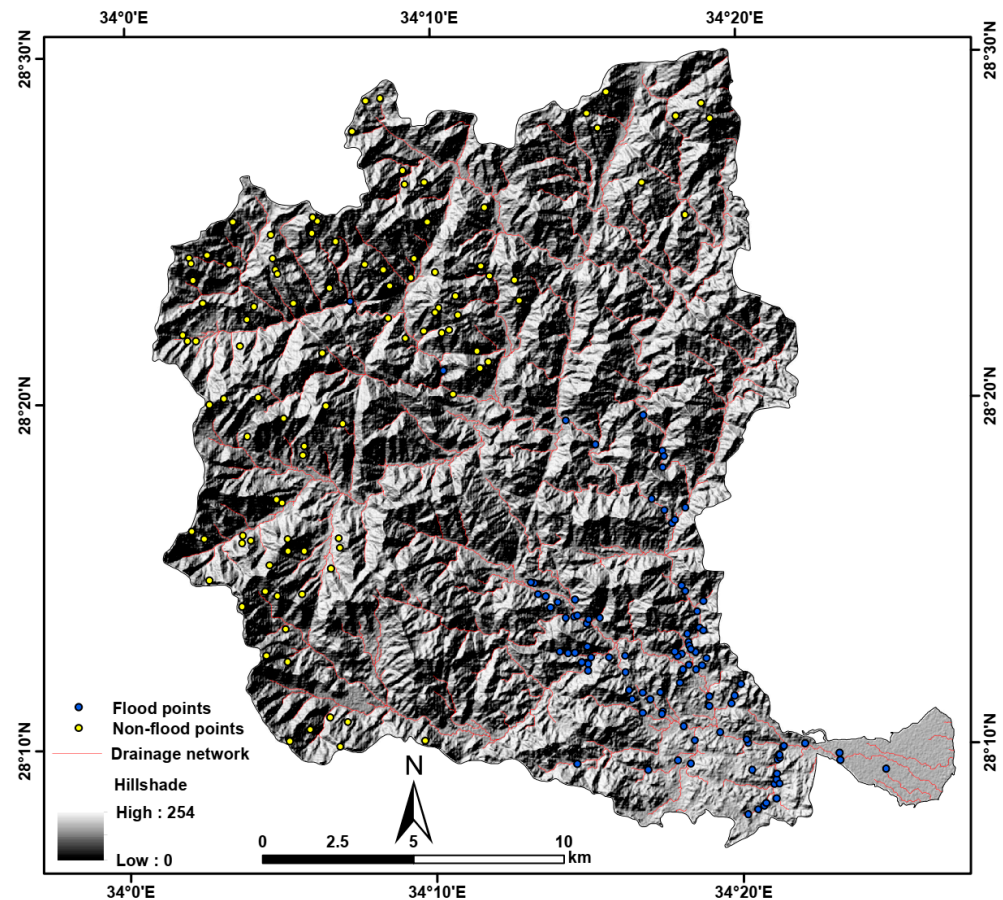


Figure 2. Validation using randomly selected 100 flood points and 100 non-flood points from the total flash flood inventory map of Wadi Kid, southeastern Sinai.

2.2.3. Definition of the Flash Flood Triggering Factors

The hydrogeomorphic characteristics of Wadi Kid were thoroughly studied, and nineteen potential factors that can trigger flash floods were identified based on previous literature (e.g., [42–53,76–78]) and the fieldwork experience in the area of study. These geospatial layers (Tables 2 and 3) included elevation (E), vertical flow distance (VFD), horizontal flow distance (HFD), topographic wetness index (TWI), distance from Wadis (DfW), flow length in the upstream (FL_UP), relative slope position (RSP), convergence index (CI), profile curvature (Pfc), stream transport index (STI), rainfall (RF), slope (S), drainage density (DD), landforms (LF), geology (G), height above the nearest drainage network (HAND), Melton ruggedness number (MRN), plan curvature (PnC), and stream power index (SPI). Following this, the PCA algorithm was employed to select nine less correlated variables (i.e., RF, S, DD, LF, G, HAND, MRN, PnC, and SPI) (Table 3 and Figure 3) and to eliminate multicollinearity between them.

Each factor was resampled to the spatial resolution of 30 m, where the area of the study grid was bounded by 1431 and 1421 columns and rows, respectively. Most independent continuous variables were classified using the natural break classification algorithm [79]. This method defines the class breaks and keeps collectively similar values (i.e., lessening the variance within classes) while increasing the differences between diverse classes.

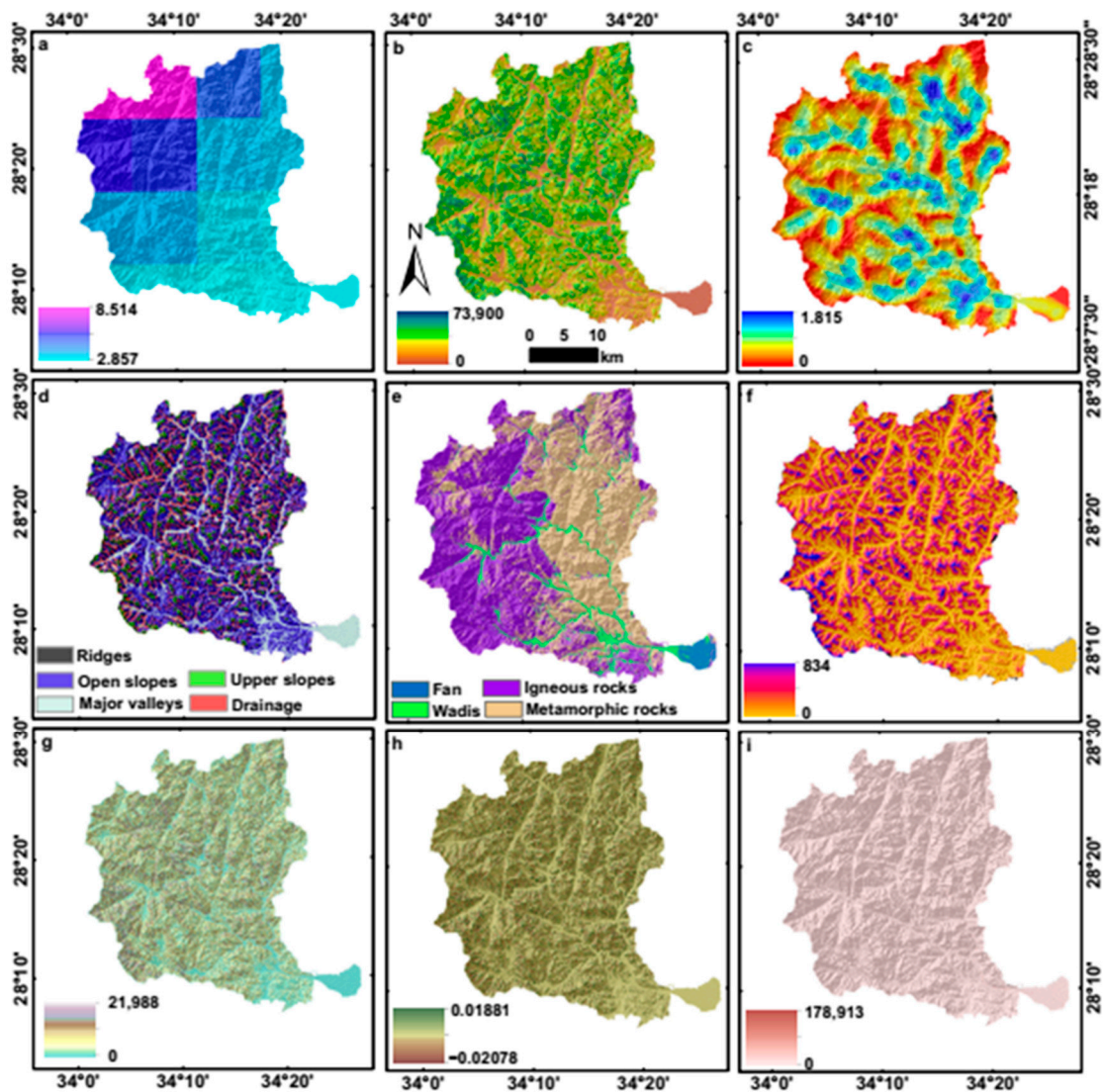


Figure 3. Flash flood triggering factors: (a) rainfall (RF) (mm/month), (b) slope (S°), (c) drainage density (DD) (km/km^2), (d) landforms (LF), (e) geology (G), (f) height above nearest drainage network (HAND) (m), (g) Melton ruggedness number (MRN) (m/m), (h) plan curvature (PnC) ($1/100$ of a z-unit), and (i) stream power index (SPI).

2.2.4. Preparation of the Satellite Precipitation Data Using NASA Giovanni Web Tool

The Global Precipitation Measurement (GPM) Mission is a joint project between the National Aeronautics and Space Administration (NASA) and the Japan Aerospace Exploration Agency (JAXA) to monitor global precipitation. The GPM spacecraft has two key instruments: a radar and a radiometer, which serve as the standard reference for other satellites' precipitation products. The mission aims to measure rainfall and snowfall using two integrated instruments: the GPM microwave imager (GMI) captures precipitation patterns and strengths, while the dual-frequency precipitation Radar (DPR) produces a three-dimensional view of precipitating particles [80]. The Integrated Multi-satellite Retrievals for GPM products (IMERG) were generated by blending the following: (i) satellite passive microwave precipitation estimates from the GPM constellation, (ii) microwave-calibrated infrared satellite measurements, (iii) rainfall gauge records, and (iv) other precipitation products of different sensors [81]. The system runs for every observation several times to generate products of 0.1° and 30-min spatial and temporal resolutions, respectively. IMERG has three different products with varying accuracy and response time [82,83], from the near real-time early IMERG to late IMERG runs to the final research-grade IMERG with 4 h,

12 h, and 3.5 months latency, respectively. The final run has the advantage of including monthly in situ gauge estimates in the validation step.

Giovanni [84] is a user-friendly online tool developed by NASA scientists for processing, analyzing, and visualizing various big satellite data (e.g., precipitation, temperature, and evaporation) on the fly without requiring downloads. The user guide delivers additional information on how to use this web tool (<https://giovanni.gsfc.nasa.gov/giovanni/doc/UsersManualworkingdocument.docx.html#h.k1vpfalyfmci>; accessed on 6 February 2023). The Giovanni web tool has successfully processed and evaluated different satellite precipitation estimates (e.g., [85–87]). In this study, we used the Giovanni web-based application to process the recurring average of level-3 GPM_3IMERGM v06 in December, January, and February from 2000 to 2021 over the study area (Figure 3a). The winter season was selected because it best represents the spatial distribution of the rainfall in mm/month over the study area.

Table 2. Definitions of initial flash flood causative variables excluded from the final flash flood susceptibility model based on employing PCA.

Variables' Definitions	
E	<ul style="list-style-type: none"> Elevation (m) is the key factor in flash flood modeling, with height playing an inverse role in flash flood likelihood [26]. Flash floods are less common at higher elevations, as they are inversely proportional to elevation [88,89]. Flat areas or lower elevations are more prone to flash floods.
VFD	<ul style="list-style-type: none"> Vertical flow distance (m) is the vertical component of flow distance. It determines the distance between each pixel in the given domain and the pixel(s) on the river or stream where they flow in a downward direction (https://pro.arcgis.com/en/pro-app/latest/help/analysis/raster-functions/flow-distance-function.htm; accessed on 6 April 2023).
HFD	<ul style="list-style-type: none"> Horizontal flow distance (m) calculates the surface flow distance in the horizontal component. It measures the distance between each pixel in the domain and the pixel(s) on the river or stream where they flow into but only in the horizontal direction (https://pro.arcgis.com/en/pro-app/latest/help/analysis/raster-functions/flow-distance-function.htm; accessed on 6 April 2023).
TWI	<ul style="list-style-type: none"> Topographic wetness is an indicator of soil moisture content and surface saturation, which can lead to floods in areas with high levels of saturation [90,91]. As the level of saturation increases, the groundwater table rises, and the zone of aeration becomes fully saturated, creating favorable conditions for flash floods. Therefore, areas with higher TWI values are more susceptible to flash floods.
DfW	<ul style="list-style-type: none"> Distance from Wadis (m). According to Rahmati et al. (2016), the proximity of a location to a river is a crucial factor that significantly affects the extent and size of floods. Generally, areas closer to rivers are at a higher risk of floods [92].
FL_UP	<ul style="list-style-type: none"> The Flow length_Upstream (m) index calculates the longest upstream (i.e., upslope) distance along the flow path for each cell, from the cell to the top of the drainage divide (https://pro.arcgis.com/en/pro-app/latest/tool-reference/spatial-analyst/flow-length.htm; accessed on 6 April 2023). It often expresses the basin's concentration time.
RSP	<ul style="list-style-type: none"> Relative slope position is the relative position of the slope's altitude to the valley and ridge elevations [93].

Table 2. Cont.

Variables' Definitions	
CI	<ul style="list-style-type: none"> The convergence index calculates the convergence and divergence values concerning overland flow [94,95].
PfC	<ul style="list-style-type: none"> Profile curvature (1/100 of a z-unit) runs parallel to the slope and shows the maximum slope's direction (https://pro.arcgis.com/en/pro-app/latest/tool-reference/spatial-analyst/how-slope-works.htm; accessed on 6 February 2023). It influences the acceleration and deceleration of the overland flow, where negative areas are at a high risk of flash floods [95].
STI	<ul style="list-style-type: none"> The stream transport index ($\text{m}^3/\text{s}/\text{km}^2$) represents the erosion and sediment transport that occurs due to flash flood propagation and can cause foundation damage [96].

Table 3. Definitions of final flash flood causative variables included in the final flash flood susceptibility model based on employing PCA.

Variables' Definitions	
RF	<ul style="list-style-type: none"> The final IMERG v06 (mm/month) is used in the current research to estimate the recurring rainfall average in the winter (Figure 3a). The rainfall datasets were processed using the online Giovanni web-based application from 2000 to 2021. They are also used in the current study as a proxy of runoff.
S	<ul style="list-style-type: none"> It is the steepness at each cell of the DEM raster grid in degrees (https://pro.arcgis.com/en/pro-app/latest/tool-reference/spatial-analyst/how-slope-works.htm; accessed on 6 February 2023). It ranged from 0° near the coastline to 74° in the rugged mountains in the study area (Figure 3b).
DD	<ul style="list-style-type: none"> Drainage density (km/km^2) was extracted from PALSAR DEM 30 m. It expresses the density of the linear drainage features within the vicinity of each cell in units of length per unit of area (i.e., km/km^2) [97] (Figure 3c).
LF	<ul style="list-style-type: none"> The study area is classified into five significant landforms (i.e., major valleys, drainage, open slopes, upper slopes, and ridges) (Figure 3d).
G	<ul style="list-style-type: none"> The lithology of the study area (Figure 3e) is composed of a Kid complex (i.e., a Precambrian metamorphic belt that was intruded by granites and the gabbro–diorite complex) [5]. The Plio–Pleistocene fluvio-marine sediments (i.e., intercalations of fluvial sand, gravels, limestone bands, and shell fragments) of Nabq alluvial plain unconformably overlay the basement badlands.
HAND	<ul style="list-style-type: none"> The height above the nearest drainage (m) (Figure 3f) is a normalized DEM. It represents the relative height difference between a specific cell on the DEM surface and its hydrologically linked cell in the channel drainage network [98,99]. HAND algorithm and implementation steps can be found in Rosim et al. [100] and Rahmati et al. [101].

Table 3. Cont.

Variables' Definitions	
MRN	<ul style="list-style-type: none"> • Melton ruggedness number (m/m) (Figure 3g) is linked to the flow accumulation. • It is a morphometric index computed per pixel as the difference between the minimum and maximum altitude divided by the square root of the watershed of the area under investigation [102–104].
PnC	<ul style="list-style-type: none"> • Plan curvature (1/100 of a z-unit) (Figure 3h) is perpendicular to the direction of the maximum slope. It indicates the degree of surface slope distortion. • A positive planform implies that the surface is laterally convex at that cell, a negative value means the surface is laterally concave at that cell, and zero indicates the surface is linear (https://desktop.arcgis.com/en/arcmap/10.3/manage-data/raster-and-images/curvature-function.htm; accessed on 6 February 2023).
SPI	<ul style="list-style-type: none"> • The stream power index (Figure 3i) indicates the erosive power of flowing runoff over a certain watershed area. The surface flow's power is directly proportional to the SPI [105].

2.3. Methods

The workflow of the implemented methodology in the current study is exemplified in Figure 4, and is described as follows: (i) deriving a set of possible explanatory flash flood triggering factors at a spatial resolution of 30 m, (ii) extracting the drainage network from ALOS PALSAR DEM (30 m) to prepare the other set of the independent parameters, (iii) using the NASA Giovanni web tool to extract spatial rainfall distribution, (iv) applying the principal component analysis (PCA) technique to select less correlated flash flood causative factors, (v) implementing the AHP method to estimate relative weights of the flash flood triggering factors, (vi) generating the flash flood susceptibility map, (vii) validating the developed model, and (viii) comparing flash flood susceptibility classes.

2.3.1. Principle Component Analysis (PCA)

Principle component analysis (PCA) [106] is an exploratory data analysis that was computed to reduce data dimension by transforming the most correlated factors into a new coordinate system. This new system allows for the explanation of the total variance in the data utilizing fewer dimensions than in the original data, with the first component explaining the highest variance. PCA linearly transforms the datasets into orthogonal uncorrelated principal components (PCs) while preserving the initial data's total variance, which is mathematically represented as follows:

$$PC_j = \sum_1^n a_{ij} x_i \quad j = 1, n \quad (1)$$

where PC_j are the PCs, a_{ij} denotes the scores of the linear transformation, x_i represents the flash flood triggering factors, and n is the number of factors. The principal components are the eigenvectors of the data correlation matrix, and the associated eigenvalues indicate the variance in descending order, explained by each eigenvector. The principal components with eigenvalues less than one contain less information than the initial variables, which allows for dimensionality reduction of the data.

Carnes and Slade [107] recommend using the PCA algorithm to reduce the dimensionality of any dataset as well as to quantify any interdependence between independent variables (i.e., eliminate multicollinearity among features [108]). By removing principal components linked to small eigenvalues, the dimensionality of explanatory factors can be decreased without impacting the model's predictive power, indicating that the deleted components were not critical to explaining changes in the dependent variable.

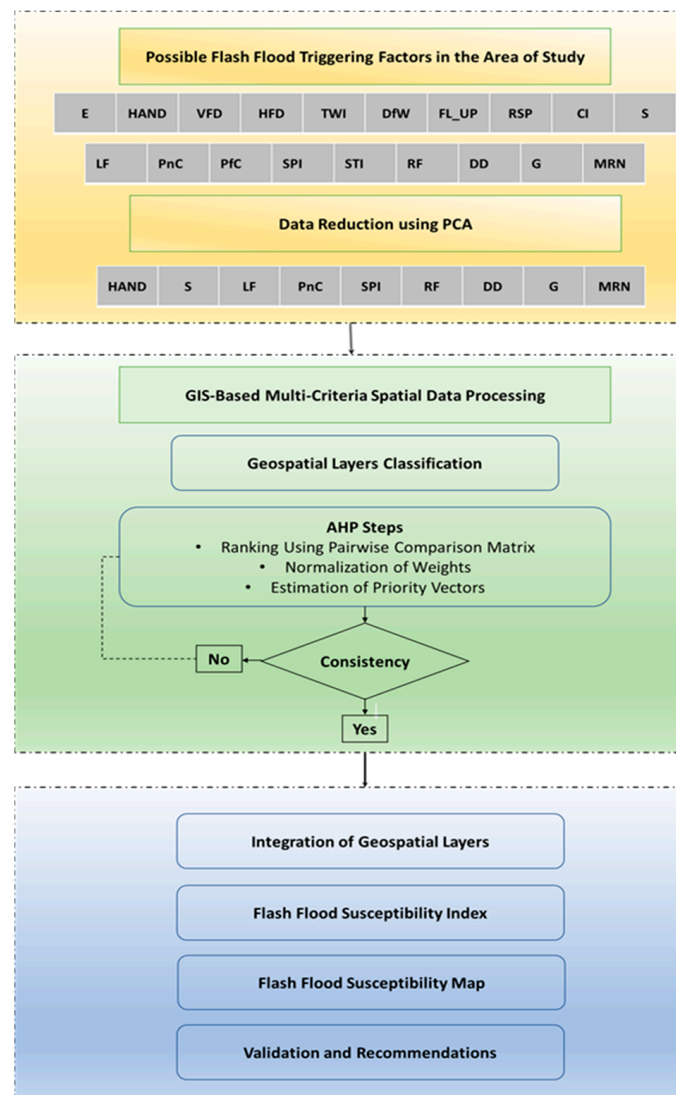


Figure 4. Methodology flowchart of the GIS-based AHP for determining flash flood prone zones along the southwestern coast of the Gulf of Aqaba, Sinai, Egypt. The flood triggering factors are elevation (E) (m), height above nearest drainage network (HAND) (m), vertical flow distance (VFD) (m), horizontal flow distance (HFD) (m), topographic wetness index (TWI), distance from a drainage Wadis (DfW) (m), flow length in the upstream (FL_UP) (m), relative slope position (RSP), convergence index (CI), slope (S°), landforms (LF), plan curvature (PnC) (1/100 of a z-unit), profile curvature (Pfc) (1/100 of a z-unit), stream power index (SPI), stream transport index (STI) ($\text{m}^3/\text{s}/\text{km}^2$), rainfall (RF) (mm/month), drainage density (DD) (km/km^2), geology (G), and the Melton ruggedness number (MRN) (m/m).

2.3.2. Analytical Hierarchy Process (AHP)

Multiple-criteria decision-making (MCDM) introduces various methods for solving different decision problems [36]. AHP was developed by Saaty et al. [39] as an MCDM technique to solve various types of decision problems based on relative preferences allocated per individual criterion to accomplish a specific purpose. It is a structural technique for developing a numerical score to rank each decision alternative based on how well each alternative meets the decision maker's criteria (i.e., priority) of each factor. In Saaty's AHP [39], a pairwise comparison matrix is employed to estimate relative weighting coefficients for each criterion from the eigenvectors of these factors by applying a ranking scale between 1 and 9 (Table 4). This matrix is evaluated using a random consistency index [39].

Table 4. Saaty’s relative importance scale value and Random consistency index value.

Saaty’s Relative Importance Scale Value															
Less Important								More Important							
Extremely	Very Strongly	Strongly	Moderately	Equal	Moderately	Strongly	Very Strongly	Extremely							
1/9	1/7	1/5	1/3	1	3	5	7	9							
2, 4, 6, and 8 are the intermediary values between the two adjoining judgments in a pairwise comparison matrix															
Random Consistency Index Value															
Consistency Ratio Table															
n	1	2	3	4	5	6	7	8	9	10	11	12	13	14	15
RI	0.00	0.00	0.58	0.90	1.12	1.24	1.32	1.41	1.45	1.49	1.51	1.48	1.56	1.57	1.59

The detailed steps for applying the GIS-based AHP model for flash flood susceptibility modeling in the current area of study were to (i) define the decision problem (i.e., flash flood susceptibility) and establish the conceptual framework and the decision hierarchy; (ii) collect information from expert researchers about flood triggering factors through the scholarly literature. We also depend on our previous experience studying flash floods in the current area and similar locations to identify the initial triggering factors. Nineteen flood causative factors were initially selected, but they were later reduced to nine variables using PCA, including rainfall (RF) (mm/month), slope (S°), drainage density (DD) (km/km²), geology (G), height above nearest drainage network (HAND) (m), landforms (LF), Melton ruggedness number (MRN) (m/m), plan curvature (PnC) (1/100 of a z-unit), and stream power index (SPI); (iii) employ a pairwise comparison matrix between flash flood triggering factors based on a ranking scale range from 1 to 9 (Table 4) [39]. A value of 1 indicates that the two variables being assessed are of equal priority (i.e., importance), while a value of 9 signifies that the variable in the row is much more significant for the decision problem than the variable in the column. The number of comparisons depends on the number of flash flood conditioning factors. The current study used a 9 by 9 reciprocal matrix from the paired comparison. Then, we normalized relative weights and estimated the principal eigenvector (i.e., priority vector) to determine the priority of the included factors to flash flood occurrence. Priority vector displays relative weights among the comparable factors (i.e., rank); and (iv) calculate consistency ratio (CR) (Equation (3)) (i.e., the ratio between consistency index (CI) (Equation (4)) and random consistency index (RI)). The RI (Table 4) changed per the number of variables or different matrix orders [109]. Once judgments have been entered into the pairwise comparison matrix, it is necessary to check if they are consistent. Since the numeric values were derived based on the expertise of the previous researchers, it is impossible to avoid some inconsistencies in the final judgment matrix. The CR should be less than 10% in the AHP analysis, and the weightage of the pairwise comparison matrix should be recomputed if the CR is higher than 0.1.

$$CR = \frac{CI}{RI} \tag{2}$$

$$CI = \frac{\lambda_{max} - n}{n - 1} \tag{3}$$

where CR, CI, λ_{max} , n, and RI denote the consistency ratio, consistency index, maximum eigenvalue, number of criteria or factors being compared, and random consistency index, respectively. Finally, once the CR is acceptable for a pairwise comparison matrix, the factors can be finalized based on their relative weights in relation to flash flood occurrences.

2.3.3. Flood Susceptibility Zonation

To determine the susceptibility zonation in the Wadi Kid watershed, the relative weights of flash flood triggering factors were used to calculate the flood risk index at a 30×30 m spatial resolution. The GIS-based AHP was estimated based on the significance priority of the factors using Equations (4) and (5), which are represented below:

$$FFHI = \sum_{i=1}^n W_i X_i \quad (4)$$

where FFHI is the flash flood susceptibility zonation and W_i denotes the weight of each factor; X_i corresponds to the rating of each sub-factor, and n is equal to the number of causative factors. Equation (4) can also be expressed in a more detailed form using Equation (5):

$$FFHI = W_{RF}X_{RF} + W_S X_S + W_{DD}X_{DD} + W_G X_G + W_{HAND}X_{HAND} + W_{LF}X_{LF} + W_{MRN}X_{MRN} + W_{PnC}X_{PnC} + W_{SPI}X_{SPI} \quad (5)$$

where W refers to the weight of each flood curative factor (i.e., rainfall (RF) (mm/month), slope (S°), drainage density (DD) (km/km^2), geology (G), height above nearest drainage network (HAND) (m), landforms (LF), Melton ruggedness number (MRN) (m/m), plan curvature (PnC) (1/100 of a z-unit), and stream power index (SPI)), while X denotes each sub-factor rating.

2.3.4. Accuracy Assessment of the Susceptibility Model

The area under the receiver operating characteristic (AUC ROC) evaluation metric is employed to estimate the developed model's prediction. The introduced model cannot explain the flash flood variability if the AUC is equal to or less than 0.5. Conversely, if the AUC value is closer to one, the developed model is excellent in predicting flash flood prone areas. In the present study, the AUC ROC was used to evaluate the prediction accuracy of the developed flash flood susceptibility outputs. This method has been successfully employed in several studies (e.g., [37,44]) to assess the performance of the GIS-based AHP models for flash flood susceptibility. The AUC value ranges from 0.00 to 1.00 and is classified into five categories: low, moderate, good, very good, and excellent accuracy, corresponding to 0.50 to 0.60, 0.61 to 0.70, 0.71 to 0.80, 0.81 to 0.90, and 0.91 to 1.00, respectively. The developed FFHI model was validated using the random flood and non-flood points (Figure 2) extracted from the total flood inventory map of the study area.

The two-dimensional AUC ROC graph illustrates the trade-off between the false positive rate (FPR) (i.e., $1 - \text{specificity}$) on the X-axis and the true positive rate (TPR) (i.e., sensitivity) on the Y-axis [110]. These are represented in Equations (6) and (7), which are as follows:

$$X = 1 - \text{Specificity} = 1 - \left[\frac{TN}{TN + FP} \right] \quad (6)$$

$$Y = \text{Sensitivity} = \left[\frac{TP}{TP + FN} \right] \quad (7)$$

TN, FP, TP, and FN represent true negative, false positive, true positive, and false negative, respectively [111].

3. Results

3.1. Principal Component Analysis (PCA)

Tables 5 and 6 display the results of the PCA conducted on the nineteen flash flood triggering factors. Table 5 shows the loading values of each factor in the nineteen principal components estimated by employing the PCA method (i.e., PC1, PC2, PC3, PC19). For example, the factor responsible for the highest loading might signify a specific PC of interest [112]. The loading values of each factor are classified into three categories (i.e.,

strong > 0.75 , $0.75 >$ moderate > 0.5 , and $0.5 >$ weak > 0.4) [113,114], with loading values less than 0.50 not considered significant. Table 6 lists the eigenvalues, variance, and cumulative variance explained by each principal component of the flash flood triggering factors, and significant values were indicated in bold. Only the first six principal components have eigenvalues greater than one (e.g., [112,115,116]), and are considered the main components that captured 72.838% of the variability in the data. Despite the eigenvalues from seven to ten being lower than one, the first ten PCs, accounting for 88.767% of the variation in the dataset, were considered for selecting the final flash flood triggering factors. Based on the PCA analysis (Tables 5 and 6), we reduced the dimensionality and eliminated the multicollinearity among datasets. For developing our flash flood susceptibility model, we selected HAND, S, SPI, RF, PnC, G, DD, MRN, and LF, as they are a set of factors with relatively low correlation.

3.2. Assignment of Weight and Rank to Each Flash Flood Triggering Factor

The current study applied the AHP method to weigh each flash flood triggering factor and its corresponding classes. Table 7 shows an example of a reciprocal pairwise comparison matrix for flash flood causative factors. To execute this technique, evaluating and rating each variable against every other variable is essential using Saaty's 9-point rating scale [39]. Then, the normalized relative weights and the priority vectors for each factor and its classes were estimated (Table 8) to ensure that the weights are normalized and that the sum of all weights is equal to 1 as well as to estimate the priorities of the flash triggering factors and their corresponding classes. A higher priority value indicates that a factor is more significant than others in triggering flash floods. It is impossible to entirely avoid inconsistencies in the final matrix of judgment. Therefore, inconsistency of less than 10% is allowed in the AHP analysis; otherwise, the weightage of the pairwise comparison matrix should be recomputed. The overall consistency ratio in the developed model was equal to 0.025037 (i.e., the consistency ratio was equal to 3%), which indicated that the weightage suggested for the flash flood causative factors in the pairwise comparison matrix is acceptable. The CRs % were approximately equal to 2% (RF), 8% (S), 4% (DD), 6% (G), 2% (HAND), 4% (LF), 6% (MRN), 2% (PnC), and 7% (SPI). Table 9 shows the weights of each flash flood causative factor and its subclasses based on implementing the AHP method. The weights of each variable were ranked in descending order (Table 9), with rainfall (RF = 0.310) having the highest weight, followed by slope (S = 0.221), drainage density (DD = 0.158), geology (G = 0.107), height above nearest drainage network (HAND = 0.074), landforms (LF = 0.051), Melton ruggedness number (MRN = 0.035), plan curvature (PnC = 0.022), and stream power index (SPI = 0.022).

3.3. Mapping of Flash Flood Susceptibility Zonation Using AHP Model Outputs

The main goal of this research is to develop the flash flood susceptibility zonation based on the relative priority of nine hydrogeomorphic parameters using AHP weights. The findings showed that RF and S were the most influential factors in determining flash flood zonation in Wadi Kid (Table 9), while MRN, PnC, and SPI were the less significant variables (Table 9). First, the relative weight of each flash flood triggering factor was integrated by the rating of each corresponding sub-criteria. Then, by integrating the relative weighting sum of all causative parameters, as well as the rating for each sub-criteria, the final flash flood susceptibility map (Figure 5) was generated with an overall CR value of less than 3% (<10%, validated model).

Table 5. The loading values of each flash flood triggering factor in the nineteen principal components were estimated using the PCA algorithm (significant values are indicated in bold).

Variable	PC ₁	PC ₂	PC ₃	PC ₄	PC ₅	PC ₆	PC ₇	PC ₈	PC ₉	PC ₁₀	PC ₁₁	PC ₁₂	PC ₁₃	PC ₁₄	PC ₁₅	PC ₁₆	PC ₁₇	PC ₁₈	PC ₁₉
HAND	0.84	0.13	0.15	0.32	−0.07	0.08	0.09	0.07	0.07	−0.12	0.18	0.00	−0.10	−0.12	0.01	−0.06	0.10	0.01	0.15
VFD	0.83	0.16	0.14	0.35	−0.08	0.02	0.09	0.06	0.10	−0.12	0.20	−0.01	−0.10	−0.09	0.01	−0.05	0.08	−0.02	−0.15
HFD	0.76	−0.12	0.23	0.12	0.06	0.40	0.18	0.19	−0.13	−0.07	0.01	0.03	−0.01	0.02	−0.03	0.05	−0.29	0.01	0.00
DfW	0.76	−0.10	0.19	0.02	0.08	0.36	0.12	0.13	−0.21	0.08	−0.21	−0.04	0.21	0.17	0.04	0.12	0.19	−0.01	0.00
TWI	−0.73	−0.31	0.02	0.01	0.07	0.09	0.10	0.14	−0.01	−0.41	0.20	−0.14	−0.04	0.26	−0.18	−0.01	0.04	0.01	0.00
FL_US	−0.67	−0.02	0.52	0.19	−0.18	−0.08	−0.03	0.08	0.00	−0.25	0.05	0.05	0.14	0.03	0.34	0.02	−0.03	−0.05	0.01
RSP	0.64	0.22	0.04	0.34	−0.17	−0.39	−0.20	−0.07	0.14	0.06	0.05	0.25	0.09	0.31	−0.08	0.01	−0.04	0.00	0.01
DEM	−0.56	0.17	−0.18	0.55	0.41	0.06	−0.13	−0.01	0.03	0.02	0.07	0.05	−0.04	−0.08	−0.01	0.34	0.01	0.03	0.00
CI	0.48	−0.01	0.43	−0.33	0.45	−0.17	−0.25	0.07	0.00	0.07	−0.01	−0.11	−0.35	0.15	0.13	0.04	0.00	0.00	0.00
S	0.26	0.80	−0.09	−0.13	0.01	−0.03	−0.05	−0.16	−0.06	0.08	0.24	−0.36	0.20	0.05	0.03	0.04	−0.05	0.00	0.01
LF	−0.15	−0.74	0.07	−0.04	0.00	0.12	−0.08	0.23	0.20	0.44	0.34	−0.02	0.10	0.01	0.03	−0.01	0.01	−0.01	0.00
PfC	−0.34	0.55	0.01	−0.43	0.21	0.28	0.12	−0.04	−0.23	0.05	0.26	0.34	−0.03	0.04	0.03	−0.04	0.04	0.01	−0.01
SPI	−0.49	0.19	0.76	0.15	−0.26	−0.01	0.01	0.03	−0.08	0.13	−0.04	−0.05	−0.01	−0.01	−0.04	−0.04	0.02	0.16	−0.02
STI	−0.53	0.32	0.68	0.14	−0.15	0.04	0.04	0.00	−0.05	0.20	−0.05	−0.02	−0.09	−0.03	−0.19	0.02	0.00	−0.13	0.01
RF	−0.36	0.08	−0.13	0.61	0.51	0.25	−0.20	−0.09	−0.09	0.10	−0.08	−0.04	0.02	0.07	0.04	−0.28	−0.01	−0.01	0.00
PnC	0.32	−0.16	0.49	−0.23	0.53	−0.24	−0.29	0.07	−0.04	−0.19	0.03	0.06	0.26	−0.18	−0.14	−0.03	0.00	0.00	0.00
DD	−0.02	−0.13	0.18	0.10	0.45	−0.37	0.73	−0.22	0.09	0.10	0.00	−0.01	0.04	0.03	0.03	−0.01	−0.01	0.00	0.00
G	0.16	−0.29	0.32	−0.11	−0.03	0.41	−0.12	−0.71	0.28	−0.08	0.02	0.02	0.00	0.02	0.00	0.04	0.00	0.00	0.00
MRN	−0.20	0.56	0.03	−0.19	0.17	0.23	0.07	0.32	0.63	−0.04	−0.15	0.02	0.05	0.03	0.00	−0.03	0.00	0.01	0.00

Table 6. Eigenvalues, percentage of variance, and cumulative variance that are explained by each principal component.

	Initial Eigenvalues			Extraction Sums of Squared Loadings		
	Total	% of Variance	Cumulative %	Total	% of Variance	Cumulative %
1	5.507	28.983	28.983	5.507	28.983	28.983
2	2.302	12.118	41.102	2.302	12.118	41.102
3	2.054	10.810	51.912	2.054	10.810	51.912
4	1.540	8.104	60.015	1.540	8.104	60.015
5	1.359	7.155	67.171	1.359	7.155	67.171
6	1.077	5.667	72.838	1.077	5.667	72.838
7	0.891	4.692	77.530	0.891	4.692	77.530
8	0.849	4.469	81.999	0.849	4.469	81.999
9	0.691	3.637	85.636	0.691	3.637	85.636
10	0.595	3.131	88.767	0.595	3.131	88.767
11	0.439	2.308	91.076	0.439	2.308	91.076
12	0.356	1.872	92.948	0.356	1.872	92.948
13	0.350	1.843	94.791	0.350	1.843	94.791
14	0.291	1.529	96.320	0.291	1.529	96.320
15	0.238	1.254	97.574	0.238	1.254	97.574
16	0.224	1.177	98.751	0.224	1.177	98.751
17	0.145	0.762	99.514	0.145	0.762	99.514
18	0.048	0.250	99.764	0.048	0.250	99.764
19	0.045	0.236	100.000	0.045	0.236	100.000

Table 7. Pairwise comparison matrix for the nine flash flood triggering factors using Saaty's AHP method.

	RF	S	DD	G	HAND	LF	MRN	PnC	SPI
RF	1.00	2.00	3.00	4.00	5.00	6.00	7.00	9.00	9.00
S	0.500	1.00	2.00	3.00	4.00	5.00	6.00	8.00	8.00
DD	0.333	0.500	1.00	2.00	3.00	4.00	5.00	7.00	7.00
G	0.250	0.333	0.500	1.00	2.00	3.00	4.00	5.00	5.00
HAND	0.200	0.250	0.333	0.500	1.00	2.00	3.00	4.00	4.00
LF	0.167	0.200	0.250	0.333	0.500	1.00	2.00	3.00	3.00
MRN	0.143	0.167	0.200	0.250	0.333	0.500	1.00	2.00	2.00
PnC	0.111	0.125	0.143	0.200	0.250	0.333	0.500	1.00	1.00
SPI	0.111	0.125	0.143	0.200	0.250	0.333	0.500	1.000	1.00

Table 8. Normalized weights of the flash flood triggering factors.

	RF	S	DD	G	HAND	LF	MRN	PnC	SPI	Priority Vector
RF	0.355	0.426	0.396	0.348	0.306	0.271	0.241	0.225	0.225	0.310
S	0.178	0.213	0.264	0.261	0.245	0.226	0.207	0.200	0.200	0.221
DD	0.118	0.106	0.132	0.174	0.184	0.180	0.172	0.175	0.175	0.158
G	0.089	0.071	0.066	0.087	0.122	0.135	0.138	0.125	0.125	0.107
HAND	0.071	0.053	0.044	0.044	0.061	0.090	0.103	0.100	0.100	0.074
LF	0.059	0.043	0.033	0.029	0.031	0.045	0.069	0.075	0.075	0.051
MRN	0.051	0.035	0.026	0.022	0.020	0.023	0.034	0.050	0.050	0.035
PnC	0.039	0.027	0.019	0.017	0.015	0.015	0.017	0.025	0.025	0.022
SPI	0.039	0.027	0.019	0.017	0.015	0.015	0.017	0.025	0.025	0.022

Table 9. Sub-criteria of each parameter and the pairwise comparison matrix and their weights. AHP rating of sub-criteria for flood susceptibility analysis. VL, L, M, H, and VH denote very low, low, moderate, high, and very high flash flood risk classes, respectively.

V	Reclass Code	AHP Weight	Range	Flood Level	Area km ²	Area %	Rating	CR
RF	1	0.310	2.86–2.97	VH	150.971	14.582	0.416	0.015
	2		2.98–3.06	H	50.357	4.864	0.262	
	3		3.07–3.57	M	473.942	45.779	0.161	
	4		3.58–5.27	L	273.779	26.445	0.099	
	5		5.28–8.51	VL	86.234	8.33	0.062	
S	1	0.221	0–9.85	VH	188.715	18.335	0.460	0.079
	2		9.86–19.42	H	246.413	23.94	0.260	
	3		19.43–27.82	M	284.936	27.683	0.152	
	4		27.83–37.09	L	218.939	21.271	0.089	
	5		37.10–73.90	VL	90.274	8.771	0.039	
DD	1	0.158	0.00–0.22	VL	221.493	21.394	0.048	0.044
	2		0.23–0.48	L	239.81	23.163	0.075	
	3		0.49–0.73	M	262.139	25.32	0.118	
	4		0.74–1.01	H	210.21	20.304	0.239	
	5		1.02–1.82	VH	101.65	9.819	0.520	
G	1	0.107	Fan	VH	18.24	1.763	0.534	0.059
	2		Alluvial Deposits	H	72.925	7.050	0.282	
	4		Igneous Rocks	L	467.77	45.22	0.108	
	5		Metamorphic Rocks	VL	475.502	45.967	0.075	
HAND	1	0.074	0.00–55.00	VH	401.825	39.47	0.505	0.024
	2		55.01–130.00	H	265.577	26.087	0.254	
	3		130.01–219.00	M	194.994	19.153	0.123	
	4		219.01–337.00	L	116.51	11.444	0.072	
	5		337.01–834.00	VL	39.153	3.846	0.047	
LF	1	0.051	Major Valleys	VH	152.4276	14.72293	0.478	0.036
	2		Drainage Network	H	148.2786	14.32218	0.277	
	3		Open Slopes	M	496.1889	47.9267	0.129	
	4		Upper Slopes	L	68.4288	6.609513	0.075	
	5		Ridges	VL	169.9839	16.41868	0.041	
MRN	1	0.035	0.00–1.29	VH	372.2454	35.955	0.606582	0.056
	2		1.30–3.62	H	260.2377	25.136	0.15414	
	3		3.63–5.95	M	225.8541	21.815	0.130443	
	4		5.96–8.97	L	134.4015	12.982	0.064593	
	5		8.98–21.99	VL	42.5691	4.112	0.044243	
PnC	1	0.022	−0.020772–0.000611	H	167.7762	16.20544	0.239488	0.016
	2		−0.000611–0.00005	VH	344.4903	33.27419	0.623225	
	3		0.00005–0.018805	L	523.0413	50.52037	0.137288	
SPI	1	0.022	0.000	VH	274.1265	26.478	0.445213	0.070
	2		0.001–702	H	753.4431	72.775	0.299367	
	3		703–2100	M	3.6423	0.352	0.148973	
	4		2110–7020	L	2.3238	0.224	0.063601	
	5		7030–179,000	VL	1.7721	0.171	0.042847	

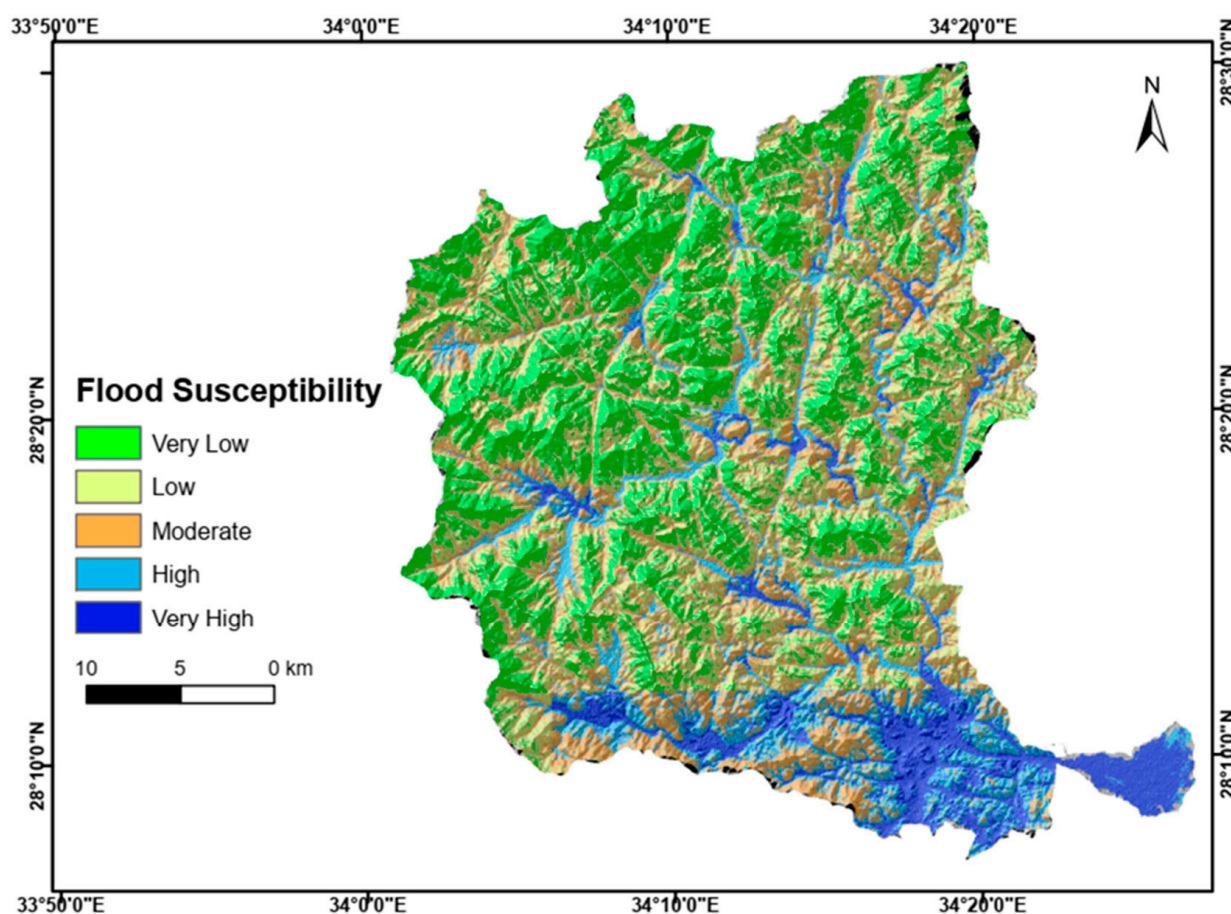


Figure 5. The developed flash flood susceptibility map at Wadi Kid, southeastern Sinai, Egypt.

Overall, the very low, low, moderate, high, and very high flash flood vulnerable areas cover approximately 28.3%, 30.9%, 19.8%, 12.8%, and 8.2% of the study area, respectively (Figure 5). The natural breaks algorithm classified the flash flood prone areas into five categories (Figure 5). The very high and high flash flood probability zones (Figure 5) were mainly located in the major Wadis and downstream areas until reaching the Wadi Kid alluvial fan. In comparison, the low and very low flash flood probability zones were mainly found in the upstream area and in rugged elevated badlands across the study area (Figure 5).

3.4. Accuracy Assessment of the GIS-Based AHP Flash Flood Susceptibility Model

Model validation is a mandatory step to ensure the accuracy of the developed flash flood susceptibility map. The current study applied the AUC metric to verify the flood susceptibility index map. The accuracy of the flash flood susceptibility map was validated by comparing it with random flood and non-flood points, and the AUC represented the map prediction accuracy. The ArcSDM tool in the ArcGIS environment exhibits an AUC with an accuracy rate greater than 0.9 (Figure 6). The observed accuracy of the GIS-based AHP model for determining flash flood prone areas is 0.916 (91.60%) (Figure 6). Therefore, the developed model successfully generated an accurate flash flood susceptibility map (Figure 5).

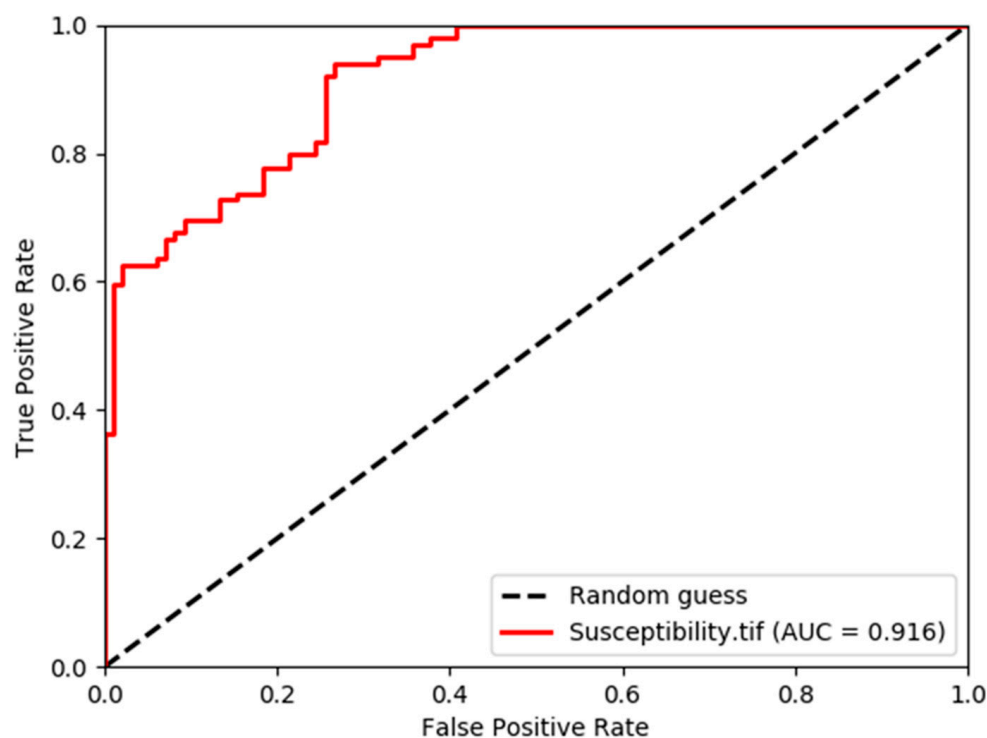


Figure 6. Validation of GIS-based AHP for flash flood susceptibility model using AUC ROC curve.

4. Discussion

Identifying areas at risk of flash floods is fundamental in implementing effective measures to mitigate and reduce flood hazards in highly vulnerable ungauged regions. Therefore, the final flash flood susceptibility map was categorized into distinct classes using a natural break classification approach, as depicted in Figure 5. This approach detects class breaks, and subsequently groups similar values together, thus minimizing variance within classes while maximizing differences between them [79].

4.1. Comparison of the Current Findings with the Prior Studies

There is no agreement on the optimal number of triggering factors required to develop a realistic flash flood susceptibility map. The current study selected nine causative parameters for susceptibility modeling, while Tehrany et al. [117] utilized thirteen variables. Bui et al. [12] and Khosravi et al. [118] used ten variables. Table 1 shows that different authors used 6 factors (e.g., [38,43,44]) and 8 factors (e.g., [45–47,50]) to develop their AHP-based flash flood susceptibility models, while Radwan et al. [53], Dano [49], and M Amen et al. [51] used 5, 4, and 12 factors, respectively. Mahmoud and Gan [119] suggested using more than six variables to avoid predicting erroneous flash flood prone areas that may be influenced by a single weight of a particular factor.

In fact, there is no flash flood in the arid areas without rainfall occurrences. In the current study, the RF was the most critical factor (Table 9) in initiating the flash flood, and had the highest weight among other flash flood triggering factors compared to other studies. This finding was consistent with other studies conducted in the Shatt Al-Arab basin, Iraq–Iran [46], Dammam [49], and Riyadh, Saudi Arabia [53] (Table 1), where RF ranked first among other flash flood triggering factors. Other studies did not include rainfall in their developed susceptibility model, such as Youssef and Hegab in Ras Gharib, Egypt [38], and Elkharchy in Najran, Saudi Arabia [42] (Table 1). The rainfall came in the third rank (e.g., [43,44]) and fourth rank (e.g., [45,50]), among other flash flood causative factors.

For validation purposes, many authors did not use a statistical evaluation metric to assess the performance of their developed flash flood susceptibility models (e.g., [47,49,53]). Some studies employed pre- and post-optical Landsat TM 8-derived NDWI and NDVI to

validate the flash flood risk map [43] and Terra MODIS/surface reflectance MOD09GA [46]. However, the effectiveness of this approach may be limited by cloud coverage, as mentioned in [54]. The proposed model scored 91.6% prediction accuracy based on the AUC evaluation metric, while Youssef and Hegab [38], Bouamrane et al. [44], and Abdelkarim et al. [50] achieved 83% (Ras Gharib, Egypt), 93.61% (Biskra basin, Algeria), and 97.1% (Al-Qurayyat, Saudi Arabia) accuracies, respectively.

4.2. Significance of the Selected Flash Flood Triggering Factors in the Current Study

The current study identified the most influential flash flood triggering factors, with RF, S, DD, G, and HAND having the highest relative weights in initiating and accelerating flash floods in the study area. HAND and LF were also significant, while MRN, PnC, and SPI were less significant. The current findings were generally in agreement with some previous studies carried out in Egypt (e.g., [37,38]) and other arid and semi-arid areas (e.g., Algeria [44], Kingdom of Saudi Arabia [42], and Tunisia [47]).

Most major valleys and downstream regions lie in zones with gentle slopes, which receive the accumulated runoff from the upper and moderate stream zones (Figure 3b). As illustrated in Figure 3c, areas with a higher density of drainage networks are more susceptible to flooding [120]. Lithologic units in the study area (Figure 3e) play an essential role in determining the flash flood risk degree associated with rocks' permeability. The flash flood hazard degree is increased in the areas dominated by major valleys (i.e., sedimentary rocks) that cut across the highly elevated and steep-sloped basement rocks (i.e., igneous and metamorphic rocks) (Figure 3e).

In addition, the alluvial fan at the lower part of the downstream constitutes a very high flash flood zone, where most of the surface water reaches the lower lands (Figure 3e). According to the present study, HAND was identified as a significant factor contributing to flash floods, and its relative weight highlighted its importance (Table 9 and Figure 3h).

The zone with saturation excess overland flow, which experienced waterlogging due to low draining potential and proximity to the groundwater table, was dominated by low HAND values [121,122]. Moreover, the current study introduced geomorphic landforms as a crucial factor in identifying areas prone to flash floods. For example, ridges (Figure 3d), typically associated with the summits of mountains and considered to be very low or low flood zones, were found to have a low likelihood of significant surface runoff due to the limited rainfall accumulation.

4.3. Pros and Cons of the Developed AHP-Based Flash Flood Susceptibility Model

The pros of AHP [123] involve the direct integration of consistent experts' judgments, the intuitive hierarchical modeling of the problem (i.e., hierarchy structure that can easily adjust to fit many sized problems [124]), automated computation of priorities and inconsistency ratios, various techniques to handle the sensitivity analyses, and the possibility of integrating GIS techniques. In contrast, the cons include the complexity of handling many pairwise comparisons and gathering information from different experts [123].

It is worth mentioning that the proposed model in the current study was able to overcome three limitations of the AHP method: (i) rank reversal [125] (i.e., aggregation of judgments and preferences transposed from units of different scales), where flash flood triggering factors were classified into five categories using nature breaks method based on the contribution of each sub-criteria to the flash flood occurrences; (ii) criteria independence [123] was solved through involving the collinearity diagnosis using PCA prior to pairwise comparisons to exclude highly correlated variables; and (iii) the selected flash flood triggering factors depend on a detailed literature review and our previous experience in studying flash floods in the study area and other similar regions, which eliminated the disadvantages associated with the criteria vagueness.

4.4. Mitigation of Flash Floods' Impact

Various possible strategies could be adopted to mitigate the impact of future flash floods [126–128]. Firstly, appropriate land use planning should be undertaken to avoid urban development in flash floodways, and new buildings should be constructed at an appropriate elevation while ensuring the maintenance of natural drainage systems. Secondly, structural measures including dikes, dams, embankment weirs, walls, levees, and other physical barriers could be prepared to protect against flash floods. In addition, constructing high-elevated roads and bridges can also help reduce flash flood damage. Thirdly, natural measures, such as restoring wetlands, floodplains, and other natural landforms can absorb runoff and reduce flash floods' impacts. Fourthly, education and outreach programs can be introduced to increase awareness of flash flood risks and provide information on how to prepare for and respond to flash floods for the local community. These programs may involve social media, public campaigns, and training programs for emergency responders. Finally, installing effective flash flood warning systems (e.g., weather forecasts, runoff monitoring, and rainfall measurements) can provide early warnings to affected area residents. It is worth noting that no single mitigation strategy can entirely reduce the impact of flash floods, but integrating different strategies can help mitigate the impact of future flash floods on communities and enhance their resilience to hazards.

4.5. Potential Applications of the Introduced Model

Due to the rapid social and economic development and the increased strategic importance of southern Sinai, it has become imperative to implement effective flash flood risk management. The developed flash flood susceptibility model in this study can potentially be applied to other rugged, mountainous regions in arid areas such as Egypt, Sultanate of Oman, the Kingdom of Saudi Arabia, United Arab Emirates, Yemen, Qatar, Libya, Iraq, and Kuwait, as well as semi-arid areas including Algeria, Tunisia, and Iran. Furthermore, it can be applied to monitor and predict flood zonation worldwide by modifying (i.e., adding, removing, and changing) the triggering factors based on the climatic and hydrological conditions of the area under study.

Incorporating the PCA algorithm improved the model efficiency by reducing the dimensionality of the initially selected nineteen flash flood triggering factors into nine, eliminating multicollinearity between these factors and reducing the subjectivity of experts' judgments. The introduced model also incorporates satellite precipitation data (i.e., GPM-IMERG V06) that was processed and downloaded through the NASA Giovanni web tool. Spatial rainfall distribution can be updated easily using the NASA Giovanni web tool to incorporate any future anomalies in dynamic rainfall over the arid study area. Furthermore, this user-friendly web tool provides direct access to process and download many large hydrological and meteorological datasets, which can suggest additional dynamic flash flood triggering factors that can be explored by different researchers worldwide.

To the best of our knowledge, the current study introduced nineteen initial triggering factors that have not been previously used in any other research related to flash flood susceptibility modeling. Therefore, the significance of these variables can be explored by other researchers in their models, providing additional insights into mapping and predicting areas susceptible to flash floods. Moreover, the final nine factors that were selected to develop the current model included new effective geospatial layers (e.g., HAND and landforms) that can be used by different authors in other flash flood susceptibility studies.

The AHP-based flood susceptibility model was spatially presented in the GIS environment. The findings obtained from the developed model align well with the existing flash flood inventory records (Figure 2). Therefore, these results can serve as a valuable source of information for governmental agencies to formulate effective flash flood prevention. Additionally, the spatial distribution characteristics of flash flood zones in mountainous areas can be better analyzed, visualized, and understood using GIS technology, offering a visual advantage in preparing accurate flood control measures.

It is worth mentioning that integrating AHP with different statistical and machine learning methods to predict areas prone to flooding worldwide can provide a real solution to convert categorical to numerical flood triggering variables. One-hot encoding algorithm is usually applied to convert categorical data into dummy variables, representing all discrete classes within the categorical layers. However, in most cases, these dummy variables are highly correlated [129], which increases the multicollinearity effects, leading to the development of models with low or no good performance.

Finally, the introduced approach can be a practical, efficient, flexible, and stepwise approach to studying other complex environmental problems, such as landslides, gully erosions, droughts, forest fires, groundwater potential, oil spills, crop suitability, and economic ores availability, among others, in a GIS-based MCDM environment.

5. Conclusions

The developed GIS-based AHP model has demonstrated its effectiveness in detecting and predicting difference risk classes of flash floods in the arid ungauged area of southeastern Sinai, Egypt, with a prediction accuracy of 91.6% based on the AUC metric. The CR has been computed in the proposed model to evaluate the inconsistency of the scholars' judgment, and the overall CR was equal to 0.025037 (i.e., <0.1), indicating that the estimated weights of the flash flood triggering factors were acceptable. The flash flood triggering factors were ranked in descending order based on their relative importance to flash flood susceptibility as follows: RF, S, DD, G, HAND, LF, MRN, PnC, and SPI. The results showed that high and very high flash flood risk zone covers 21% of the total area.

The major limitations to using the AHP method for flash flood susceptibility include (i) the variability in classifying the risk zones based on the considered factors, and (ii) the model findings may be affected by the scarcity of detailed dynamic rainfall, stream flow gauges, and soil moisture measurements; however, the use of the NASA Giovanni web tool can partially overcome this concern.

The proposed method can be applied in arid ungauged catchments for which insufficient information is available for flash flood susceptibility. Notwithstanding that the developed flash flood susceptibility zonation was validated using an inventory map of the study area, it is recommended to keep this map verified against future flash flood events to minimize the error margins. In addition, it is recommended to use verified volunteered geographic information for updating the flash flood inventory map. We also recommend comparing the developed model's outputs with the findings of other flash flood susceptibility methods, such as machine learning techniques (e.g., ANN, SVM, DT, and MaxEnt) or integrated AHP-machine learning methods for further validation of the current model outputs.

Finally, the proposed model can help many governmental agencies, such as emergency and disaster response services and urban planners, to mitigate flash flood impacts and better plan early warning systems in southeastern Sinai and other areas of similar climatic and topographic conditions worldwide. In addition, it is worth noting that the proposed approach can be adapted in other geographic areas of different climatic and hydrogeomorphic conditions by customizing decision elements to fit the characteristics of a particular area.

Author Contributions: Conceptualization, M.S. and Q.K.H.; methodology, M.S. and Q.K.H.; software, M.S.; validation, M.S. and Q.K.H.; formal analysis, M.S. and Q.K.H.; investigation, M.S. and Q.K.H.; writing—original draft preparation, M.S.; writing—review and editing, Q.K.H.; visualization, M.S.; supervision, Q.K.H.; funding acquisition, Q.K.H. All authors have read and agreed to the published version of the manuscript.

Funding: This study received partial funding from the Natural Sciences and Engineering Research Council of Canada—Discovery Grants program (NSERC DG) to Q. Hassan.

Data Availability Statement: The data used in this research are available in the public domain.

Acknowledgments: The authors acknowledge and appreciate the anonymous reviewers who have taken the time to read our manuscript and provide valuable feedback. In addition, they would like to thank the following: (i) the ALOS PALSAR (© JAXA/METI) DEM original data that were provided by JAXA and processed by Alaska Satellite Facility (ASF DAAC), 2017; (ii) both NASA and JAXA for providing the final run GPM-IMERG product; (iii) analyses and visualizations used in processing satellite precipitation data in this paper that were produced with the Giovanni online data system, developed and maintained by the NASA GES DISC.

Conflicts of Interest: The authors declare no conflict of interest.

References

1. Wheeler, H. Modeling Hydrological Processes in Arid and Semi Arid Areas. Wheeler, H. Modelling hydrological processes in arid and semi-arid areas: An introduction. In *Hydrological Modelling in Arid and Semi-Arid Areas*; Wheeler, H., Sorooshian, K., Sharma, K., Eds.; Cambridge University Press: Cambridge, UK, 2007; pp. 1–20. [CrossRef]
2. Youssef, A.M.; Pradhan, B.; Gaber, A.F.D.; Buchroithner, M.F. Geomorphological Hazard Analysis along the Egyptian Red Sea Coast between Safaga and Quseir. *Nat. Hazards Earth Syst. Sci.* **2009**, *9*, 751–766. [CrossRef]
3. Hong, Y.; Adhikari, P.; Gourley, J.J. Flash Flood. In *Encyclopedia of Natural Hazards*; Encyclopedia of Earth Sciences Series; Bobrowsky, P.T., Ed.; Springer: Dordrecht, The Netherlands, 2013. [CrossRef]
4. Borga, M.; Anagnostou, E.N.; Blöschl, G.; Creutin, J.D. Flash Flood Forecasting, Warning and Risk Management: The HYDRATE Project. *Environ. Sci. Policy* **2011**, *14*, 834–844. [CrossRef]
5. Taha, A.H.A.; Ibrahim, E.H.; Shalaby, A.S.; Shawky, M. Evaluation of Geological Hazards for Landuse Planning in Nabq Protectorate, Southeastern Sinai Using GIS Techniques. *Int. J. Geosci.* **2013**, *04*, 816–836. [CrossRef]
6. Schick, A.P.; Grodek, T.; Lekach, J. Sediment Management and Flood Protection of Desert Towns: Effects of Small Catchments. *Hum. Impact Eros. Sediment. Proc. Int. Symp. Rabat Morocco* **1997**, *245*, 183–189.
7. Allan, R.P.; Soden, B.J. Atmospheric Warming and the Amplification of Precipitation Extremes. *Science* **2008**, *321*, 1481–1484. [CrossRef]
8. Negm, A.M.; Omran, E.S.E. Introduction to “Flash Floods in Egypt”. In *Flash Floods in Egypt*; Springer Nature: Cham, Switzerland, 2020; pp. 3–9.
9. El Zawahry, A.; Soliman, A.H.; Bekhit, H. Critical Analysis and Design Aspects of Flash Flood in Arid Regions: Cases from Egypt and Oman. In *Flash Floods in Egypt*; Springer Nature: Cham, Switzerland, 2020; pp. 31–42.
10. USGS: What Is a Landslide Hazard Map? Available online: https://www.usgs.gov/faqs/what-a-landslide-hazard-map?qt-news_science_products=0#qt-news_science_products (accessed on 7 November 2019).
11. Meyer, V.; Scheuer, S.; Haase, D. A Multicriteria Approach for Flood Risk Mapping Exemplified at the Mulde River, Germany. *Nat. Hazards* **2009**, *48*, 17–39. [CrossRef]
12. Tien Bui, D.; Khosravi, K.; Shahabi, H.; Daggupati, P.; Adamowski, J.F.; Melesse, A.M.; Thai Pham, B.; Pourghasemi, H.R.; Mahmoudi, M.; Bahrami, S.; et al. Flood Spatial Modeling in Northern Iran Using Remote Sensing and GIS: A Comparison between Evidential Belief Functions and Its Ensemble with a Multivariate Logistic Regression Model. *Remote Sens.* **2019**, *11*, 1589. [CrossRef]
13. Rahman, M.; Ningsheng, C.; Islam, M.M.; Dewan, A.; Iqbal, J.; Washakh, R.M.A.; Shufeng, T. Flood Susceptibility Assessment in Bangladesh Using Machine Learning and Multi-Criteria Decision Analysis. *Earth Syst. Environ.* **2019**, *3*, 585–601. [CrossRef]
14. Liu, Y.B.; De Smedt, F. Flood Modeling for Complex Terrain Using GIS and Remote Sensed Information. *Water Resour. Manag.* **2005**, *19*, 605–624. [CrossRef]
15. Milewski, A.; Sultan, M.; Yan, E.; Becker, R.; Abdeldayem, A.; Soliman, F.; Gelil, K.A. A Remote Sensing Solution for Estimating Runoff and Recharge in Arid Environments. *J. Hydrol.* **2009**, *373*, 1–14. [CrossRef]
16. Giraldo Osorio, J.D.; Gabriela García galiano, S. Development of a Sub-Pixel Analysis Method Applied to Dynamic Monitoring of Floods. *Int. J. Remote Sens.* **2012**, *33*, 2277–2295. [CrossRef]
17. Regmi, A.D.; Yoshida, K.; Dhital, M.R.; Pradhan, B. Weathering and Mineralogical Variation in Gneissic Rocks and Their Effect in Sangrumba Landslide, East Nepal. *Environ. Earth Sci.* **2014**, *71*, 2711–2727. [CrossRef]
18. Mashaly, J.; Ghoneim, E. Flash Flood Hazard Using Optical, Radar, and Stereo-Pair Derived DEM: Eastern Desert, Egypt. *Remote Sens.* **2018**, *10*, 1204. [CrossRef]
19. Abuzied, S.M.; Mansour, B.M.H. Geospatial Hazard Modeling for the Delineation of Flash Flood-Prone Zones in Wadi Dahab Basin, Egypt. *J. Hydroinformatics* **2019**, *21*, 180–206. [CrossRef]
20. Abdulrazzak, M.; Elfeki, A.; Kamis, A.; Kassab, M.; Alamri, N.; Chaabani, A.; Noor, K. Flash Flood Risk Assessment in Urban Arid Environment: Case Study of Taibah and Islamic Universities’ Campuses, Medina, Kingdom of Saudi Arabia. *Geomatics Nat. Hazards Risk* **2019**, *10*, 780–796. [CrossRef]
21. Bangira, T.; Maathuis, B.H.P.; Dube, T.; Gara, T.W. Investigating Flash Floods Potential Areas Using ASCAT and TRMM Satellites in the Western Cape Province, South Africa. *Geocarto Int.* **2015**, *30*, 734–754. [CrossRef]
22. Opolot, E. Application of Remote Sensing and Geographical Information Systems in Flood Management: A Review. *Res. J. Appl. Sci. Eng. Technol.* **2013**, *6*, 1884–1894. [CrossRef]

23. Durduran, S.S. Coastline Change Assessment on Water Reservoirs Located in the Konya Basin Area, Turkey, Using Multitemporal Landsat Imagery. *Environ. Monit. Assess.* **2010**, *164*, 453–461. [CrossRef]
24. Bastawesy, M.E.; Ghamdi, K. Al Assessment and Management of the Flash Floods in Al Qaseem Area, Kingdom of Saudi Arabia. *Int. J. Water Resour. Arid. Environ.* **2013**, *2*, 146–157.
25. Lee, M.; Kang, J.; Jeon, S. Application of Frequency Ratio Model and Validation for Predictive Flooded Area Susceptibility Mapping Using GIS. In Proceedings of the 2012 IEEE International Geoscience and Remote Sensing Symposium, Munich, Germany, 22–27 July 2012; pp. 895–898. [CrossRef]
26. Tehrany, M.S.; Pradhan, B.; Jebur, M.N. Flood Susceptibility Mapping Using a Novel Ensemble Weights-of-Evidence and Support Vector Machine Models in GIS. *J. Hydrol.* **2014**, *512*, 332–343. [CrossRef]
27. Campolo, M.; Soldati, A.; Andreussi, P. Artificial Neural Network Approach to Flood Forecasting in the River Arno. *Hydrol. Sci. J.* **2003**, *48*, 381–398. [CrossRef]
28. Tehrany, M.S.; Pradhan, B.; Jebur, M.N. Spatial Prediction of Flood Susceptible Areas Using Rule Based Decision Tree (DT) and a Novel Ensemble Bivariate and Multivariate Statistical Models in GIS. *J. Hydrol.* **2013**, *504*, 69–79. [CrossRef]
29. Dwivedi, S.K.; Chandra, N.; Bahuguna, S.; Pandey, A.; Khanduri, S.; Lingwal, S.; Sharma, N.; Singh, G. Hydrometeorological Disaster Risk Assessment in Upper Gori–Ramganga Catchment, Uttarakhand, India. *Geocarto Int.* **2022**, *37*, 11998–12013. [CrossRef]
30. Lin, J.; He, P.; Yang, L.; He, X.; Lu, S.; Liu, D. Predicting Future Urban Waterlogging-Prone Areas by Coupling the Maximum Entropy and FLUS Model. *Sustain. Cities Soc.* **2022**, *80*, 103812. [CrossRef]
31. Zeng, Z.; Li, Y.; Lan, J.; Hamidi, A.R. Utilizing User-Generated Content and GIS for Flood Susceptibility Modeling in Mountainous Areas: A Case Study of Jian City in China. *Sustainability* **2021**, *13*, 6929. [CrossRef]
32. Benediktsson, J.A.; Swain, P.H.; Ersoy, O.K. Neural Network Approaches versus Statistical Methods in Classification of Multi-source Remote Sensing Data. *IEEE Trans. Geosci. Remote Sens.* **1990**, *28*, 540–552. [CrossRef]
33. Kia, M.B.; Pirasteh, S.; Pradhan, B.; Mahmud, A.R.; Sulaiman, W.N.A.; Moradi, A. An Artificial Neural Network Model for Flood Simulation Using GIS: Johor River Basin, Malaysia. *Environ. Earth Sci.* **2012**, *67*, 251–264. [CrossRef]
34. Hassan, Z.; Shamsudin, S.; Harun, S.; Malek, M.A.; Hamidon, N. Suitability of ANN Applied as a Hydrological Model Coupled with Statistical Downscaling Model: A Case Study in the Northern Area of Peninsular Malaysia. *Environ. Earth Sci.* **2015**, *74*, 463–477. [CrossRef]
35. Tehrany, M.S.; Pradhan, B.; Mansor, S.; Ahmad, N. Flood Susceptibility Assessment Using GIS-Based Support Vector Machine Model with Different Kernel Types. *Catena* **2015**, *125*, 91–101. [CrossRef]
36. Monprapussorn, S.; Thaitakoo, D.; Banomyong, R. Sustainability Framework for Hazardous Materials Transport Route Planning. *Int. J. Sustain. Soc.* **2011**, *3*, 33–51. [CrossRef]
37. Mohamed, S.A. Development of a GIS-Based Alert System to Mitigate Flash Flood Impacts in Asyut Governorate, Egypt. *Nat. Hazards* **2021**, *108*, 2739–2763. [CrossRef]
38. Youssef, A.M.; Hegab, M.A. Flood-Hazard Assessment Modeling Using Multicriteria Analysis and GIS: A Case Study—Ras Gharib Area, Egypt. In *Spatial Modeling in GIS and R for Earth and Environmental Sciences*; Elsevier: Amsterdam, The Netherlands, 2019; pp. 229–257. [CrossRef]
39. Saaty, T. *The Analytic Hierarchy Process (AHP) for Decision Making*; McGraw-Hill: London, UK, 1980; pp. 1–69.
40. Fernández, D.S.; Lutz, M.A. Urban Flood Hazard Zoning in Tucumán Province, Argentina, Using GIS and Multicriteria Decision Analysis. *Eng. Geol.* **2010**, *111*, 90–98. [CrossRef]
41. Rozos, D.; Bathrellos, G.D.; Skilodimou, H.D. Comparison of the Implementation of Rock Engineering System and Analytic Hierarchy Process Methods, upon Landslide Susceptibility Mapping, Using GIS: A Case Study from the Eastern Achaia County of Peloponnesus, Greece. *Environ. Earth Sci.* **2010**, *63*, 49–63. [CrossRef]
42. Elkhrachy, I. Flash Flood Hazard Mapping Using Satellite Images and GIS Tools: A Case Study of Najran City, Kingdom of Saudi Arabia (KSA). *Egypt. J. Remote Sens. Space Sci.* **2015**, *18*, 261–278. [CrossRef]
43. Dahri, N.; Abida, H. Monte Carlo Simulation-Aided Analytical Hierarchy Process (AHP) for Flood Susceptibility Mapping in Gabes Basin (Southeastern Tunisia). *Environ. Earth Sci.* **2017**, *76*, 1–14. [CrossRef]
44. Bouamrane, A.; Derdous, O.; Dahri, N.; Tachi, S.E.; Boutebba, K.; Bouziane, M.T. A Comparison of the Analytical Hierarchy Process and the Fuzzy Logic Approach for Flood Susceptibility Mapping in a Semi-Arid Ungauged Basin (Biskra Basin: Algeria). *Int. J. River Basin Manag.* **2020**, *20*, 203–213. [CrossRef]
45. Dhekra, S.; Lahcen, Z.; Salma, H.; Haythem, M.M.; Adel, Z.; Mahmoud, D. Correction to: GIS-Based MCDM-AHP Modeling for Flood Susceptibility Mapping of Arid Areas, Southeastern Tunisia. *Geocarto Int.* **2020**, *35*, 991–1017, Erratum in *Geocarto Int.* **2020**, *35*, I–IV. [CrossRef]
46. Allafta, H.; Opp, C. GIS-Based Multi-Criteria Analysis for Flood Prone Areas Mapping in the Trans-Boundary Shatt Al-Arab Basin, Iraq-Iran. *Geomat. Nat. Hazards Risk* **2021**, *12*, 2087–2116. Available online: <http://www.tandfonline.com/action/journalInformation?show=aimsScope&journalCode=tgnh20#.VsXodSCLRhE> (accessed on 6 April 2023). [CrossRef]
47. Hammami, S.; Zouhri, L.; Souissi, D.; Souei, A.; Zghibi, A.; Marzougui, A.; Dlala, M. Application of the GIS Based Multi-Criteria Decision Analysis and Analytical Hierarchy Process (AHP) in the Flood Susceptibility Mapping (Tunisia). *Arab. J. Geosci.* **2019**, *12*, 1–16. [CrossRef]

48. Ikkirri, M.; Faik, F.; Echogdali, F.Z.; Antunes, I.M.H.R.; Abioui, M.; Abdelrahman, K.; Fnais, M.S.; Wanaim, A.; Id-Belqas, M.; Boutaleb, S.; et al. Flood Hazard Index Application in Arid Catchments: Case of the Taguenit Wadi Watershed, Lakhssas, Morocco. *Land* **2022**, *11*, 1178. [[CrossRef](#)]
49. Dano, U.L. An AHP-Based Assessment of Flood Triggering Factors to Enhance Resiliency in Dammam, Saudi Arabia. *GeoJournal* **2021**, *87*, 1945–1960. [[CrossRef](#)]
50. Abdelkarim, A.; Al-Alola, S.S.; Alogayell, H.M.; Mohamed, S.A.; Alkadi, I.I.; Ismail, I.Y. Integration of GIS-Based Multicriteria Decision Analysis and Analytic Hierarchy Process to Assess Flood Hazard on the Al-Shamal Train Pathway in Al-Qurayyat Region, Kingdom of Saudi Arabia. *Water* **2020**, *12*, 1702. [[CrossRef](#)]
51. M Amen, A.R.; Mustafa, A.; Kareem, D.A.; Hameed, H.M.; Mirza, A.A.; Szydłowski, M.; Bala, B.K. Mapping of Flood-Prone Areas Utilizing GIS Techniques and Remote Sensing: A Case Study of Duhok, Kurdistan Region of Iraq. *Remote Sens.* **2023**, *15*, 1102. [[CrossRef](#)]
52. Elsebaie, I.H.; Kawara, A.Q.; Alnahit, A.O. Mapping and Assessment of Flood Risk in the Wadi Al-Lith Basin, Saudi Arabia. *Water* **2023**, *15*, 902. [[CrossRef](#)]
53. Radwan, F.; Alazba, A.A.; Mossad, A. Flood Risk Assessment and Mapping Using AHP in Arid and Semiarid Regions. *Acta Geophys.* **2019**, *67*, 215–229. [[CrossRef](#)]
54. Gan, T.Y.; Zunic, F.; Kuo, C.C.; Strobl, T. Flood Mapping of Danube River at Romania Using Single and Multi-Date ERS2-SAR Images. *Int. J. Appl. Earth Obs. Geoinf.* **2012**, *18*, 69–81. [[CrossRef](#)]
55. W., H.B. The Topography and Geology of the Peninsula of Sinai (Western Portion). *Nature* **1908**, *78*, 337. [[CrossRef](#)]
56. El-Rawy, M.; Elsadek, W.M.; De Smedt, F. Flash Flood Susceptibility Mapping in Sinai, Egypt Using Hydromorphic Data, Principal Component Analysis and Logistic Regression. *Water* **2022**, *14*, 2434. [[CrossRef](#)]
57. Omran, E.S.E. Egypt's Sinai Desert Cries: Flash Flood Hazard, Vulnerability, and Mitigation. In *Flash Floods in Egypt*; Springer Nature: Cham, Switzerland, 2020; pp. 215–236.
58. Ghoneim, E.; Foody, G.M. Assessing Flash Flood Hazard in an Arid Mountainous Region. *Arab. J. Geosci.* **2011**, *6*, 1191–1202. [[CrossRef](#)]
59. El-sammany, M.S. Forecasting of Flash Floods over Wadi Watier—Sinai Peninsula Using the Weather Research and Forecasting (WRF) Model. *Int. J. Geol. Environ. Eng.* **2010**, *4*, 996–1000.
60. Malamud, B.D.; Turcotte, D.L.; Guzzetti, F.; Reichenbach, P. Landslide Inventories and Their Statistical Properties. *Earth Surf. Process. Landforms* **2004**, *29*, 687–711. [[CrossRef](#)]
61. Guzzetti, F.; Carrara, A.; Cardinali, M.; Reichenbach, P. Landslide Hazard Evaluation: A Review of Current Techniques and Their Application in a Multi-Scale Study, Central Italy. *Geomorphology* **1999**, *31*, 181–216. [[CrossRef](#)]
62. Scaioni, M.; Longoni, L.; Melillo, V.; Papini, M. Remote Sensing for Landslide Investigations: An Overview of Recent Achievements and Perspectives. *Remote Sens.* **2014**, *6*, 9600–9652. [[CrossRef](#)]
63. Goodchild, M.F. Citizens as Sensors: The World of Volunteered Geography. *GeoJournal* **2007**, *69*, 211–221. [[CrossRef](#)]
64. Albuquerque, J.P.; Herfort, B.; Brenning, A.; Zipf, A. A Geographic Approach for Combining Social Media and Authoritative Data towards Identifying Useful Information for Disaster Management. *Int. J. Geogr. Inf. Sci.* **2015**, *29*, 1–23. [[CrossRef](#)]
65. Horita, F.E.A.; de Albuquerque, J.P.; Degrossi, L.C.; Mendiondo, E.M.; Ueyama, J. Development of a Spatial Decision Support System for Flood Risk Management in Brazil That Combines Volunteered Geographic Information with Wireless Sensor Networks. *Comput. Geosci.* **2015**, *80*, 84–94. [[CrossRef](#)]
66. Faizal, M.H.; Latiff, Z.A.; Iskandar, M.A.M. A Study of Volunteered Geographic Information (VGI) Assessment Methods for Flood Hazard Mapping: A Review. *J. Teknol.* **2015**, *75*, 127–134.
67. Schnebele, E.; Cervone, G. Improving Remote Sensing Flood Assessment Using Volunteered Geographical Data. *Nat. Hazards Earth Syst. Sci.* **2013**, *13*, 669–677. [[CrossRef](#)]
68. Schnebele, E.; Cervone, G.; Kumar, S.; Waters, N. Real Time Estimation of the Calgary Floods Using Limited Remote Sensing Data. *Water* **2014**, *6*, 381–398. [[CrossRef](#)]
69. Erskine, M.; Gregg, D.G. Utilizing Volunteered Geographic Information to Develop a Real-Time Disaster Mapping Tool: A Prototype and Research Framework. In Proceedings of the International Conference on Information Resources Management, Vienna, Austria, 1–23 May 2012; pp. 1–14.
70. McDougall, K. Using Volunteered Information to Map the Queensland Floods. In Proceedings of the Surveying and Spatial Sciences Conference, Wellington, New Zealand, 21–25 November 2011; pp. 13–23.
71. Tehrany, M.S.; Lee, M.-J.J.; Pradhan, B.; Jebur, M.N.; Lee, S. Flood Susceptibility Mapping Using Integrated Bivariate and Multivariate Statistical Models. *Environ. Earth Sci.* **2014**, *72*, 4001–4015. [[CrossRef](#)]
72. Tehrany, M.S.; Shabani, F.; Neamah Jebur, M.; Hong, H.; Chen, W.; Xie, X. GIS-Based Spatial Prediction of Flood Prone Areas Using Standalone Frequency Ratio, Logistic Regression, Weight of Evidence and Their Ensemble Techniques. *Geomat. Nat. Hazards Risk* **2017**, *8*, 1538–1561. [[CrossRef](#)]
73. De Smith, M.; Goodchild, M.F.; Longley, P. *A Geospatial Analysis to Principles, Techniques and Software Tools*, 5th ed.; Winchelsea Press: Winchelsea, UK, 2015.
74. Shawky, M.; Moussa, A.; Hassan, Q.K.; El-Sheimy, N. Pixel-Based Geometric Assessment of Channel Networks/Orders Derived from Global Spaceborne Digital Elevation Models. *Remote Sens.* **2019**, *11*, 235. [[CrossRef](#)]

75. Laurencelle, J.; Logan, T.; Gens, R. Alaska Satellite Facility (ASF)—Radiometrically Terrain Corrected ALOS PALSAR Products. *ASF-Alsk. Satell. Facil* **2015**, *1*, 12.
76. Popa, M.C.; Peptenatu, D.; Drăghici, C.C.; Diaconu, D.C. Flood Hazard Mapping Using the Flood and Flash-Flood Potential Index in the Buzău River Catchment, Romania. *Water* **2019**, *11*, 2116. [[CrossRef](#)]
77. Youssef, A.M.; Pradhan, B.; Sefry, S.A. Flash Flood Susceptibility Assessment in Jeddah City (Kingdom of Saudi Arabia) Using Bivariate and Multivariate Statistical Models. *Environ. Earth Sci.* **2016**, *75*, 12. [[CrossRef](#)]
78. Rehman, A.; Song, J.; Haq, F.; Mahmood, S.; Ahamad, M.I.; Basharat, M.; Sajid, M.; Mehmood, M.S. Multi-Hazard Susceptibility Assessment Using the Analytical Hierarchy Process and Frequency Ratio Techniques in the Northwest Himalayas, Pakistan. *Remote Sens.* **2022**, *14*, 554. [[CrossRef](#)]
79. Environmental Systems Research Institute (ESRI) Classifying Numerical Fields for Graduated Symbolology—Help | ArcGIS for Desktop. Available online: <https://desktop.arcgis.com/en/arcmap/10.3/map/working-with-layers/classifying-numerical-fields-for-graduated-symbols.htm> (accessed on 3 January 2023).
80. Hou, A.Y.; Kakar, R.K.; Neeck, S.; Azarbarzin, A.; Kummerow, C.D.; Kojima, M.; Oki, R.; Nakamura, K.; Iguchi, T. The Global Precipitation Measurement Mission. *Bull. Am. Meteorol. Soc.* **2014**, *95*, 701–722. [[CrossRef](#)]
81. Huffman, G.J.; NASA/GSFC; Bolvin, D.T.; Braithwaite, D.; Hsu, K.; Joyce, R.; Kidd, C.; Nelkin, E.J.; Sorooshian, S.; Tan, K.; et al. *Algorithm Theoretical Basis Document (ATBD) Version 06 NASA Global Precipitation Measurement (GPM) Integrated Multi-satellite Retrievals for GPM (IMERG) Prepared for: Global Precipitation Measurement (GPM) National Aeronautics and Space Administration (NASA); NASA Goddard Earth Sciences Data and Information Services Center: Greenbelt, MD, USA, 2020.*
82. Huffman, G.J.; Bolvin, D.T.; Nelkin, E.J.; Tan, J. *Integrated Multi-satellite Retrievals for GPM (IMERG) Technical Documentation George; NASA Goddard Earth Sciences Data and Information Services Center: Greenbelt, MD, USA, 2019.*
83. Huffman, G.J.; Bolvin, D.T.; Nelkin, E.J.; Stocker, E.F.; Tan, J. *V06 IMERG Release Notes; NASA Goddard Earth Sciences Data and Information Services Center: Greenbelt, MD, USA, 2019.*
84. Acker, J.G.; Leptoukh, G. Online Analysis Enhances Use of NASA Earth Science Data. *Eos. Trans. Am. Geophys. Union* **2007**, *88*, 14–17. [[CrossRef](#)]
85. Liu, Z.; Shie, C.L.; Li, A.; Meyer, D. NASA Global Satellite and Model Data Products and Services for Tropical Meteorology and Climatology. *Remote Sens.* **2020**, *12*, 2821. [[CrossRef](#)]
86. Liu, Z.; Ostrenga, D.; Teng, W.; Kempler, S.; Milich, L. Developing GIOVANNI-Based Online Prototypes to Intercompare TRMM-Related Global Gridded-Precipitation Products. *Comput. Geosci.* **2014**, *66*, 168–181. [[CrossRef](#)]
87. Liu, Z. Comparison of Precipitation Estimates between Version 7 3-Hourly TRMM Multi-Satellite Precipitation Analysis (TMPA) near-Real-Time and Research Products. *Atmos. Res.* **2015**, *153*, 119–133. [[CrossRef](#)]
88. Li, X.; Zhang, Q.; Shao, M.; Li, Y. A Comparison of Parameter Estimation for Distributed Hydrological Modelling Using Automatic and Manual Methods. *Adv. Mater. Res.* **2012**, 356–360, 2372–2375. [[CrossRef](#)]
89. Dodangeh, E.; Choubin, B.; Eigdir, A.N.; Nabipour, N.; Panahi, M.; Shamshirband, S.; Mosavi, A. Integrated Machine Learning Methods with Resampling Algorithms for Flood Susceptibility Prediction. *Sci. Total Environ.* **2020**, *705*, 135983. [[CrossRef](#)] [[PubMed](#)]
90. Yong, B.; Ren, L.L.; Hong, Y.; Gourley, J.J.; Chen, X.; Zhang, Y.J.; Yang, X.L.; Zhang, Z.X.; Wang, W.G. A Novel Multiple Flow Direction Algorithm for Computing the Topographic Wetness Index. *Hydrol. Res.* **2012**, *43*, 135–145. [[CrossRef](#)]
91. Ho-Hagemann, H.T.M.; Hagemann, S.; Rockel, B. On the Role of Soil Moisture in the Generation of Heavy Rainfall during the Oder Flood Event in July 1997. *Tellus Ser. A Dyn. Meteorol. Oceanogr.* **2015**, *6*, 28661. [[CrossRef](#)]
92. Das, S. Geospatial Mapping of Flood Susceptibility and Hydro-Geomorphologic Response to the Floods in Ulhas Basin, India. *Remote Sens. Appl. Soc. Environ.* **2019**, *14*, 60–74. [[CrossRef](#)]
93. Deng, H.; Wu, X.; Zhang, W.; Liu, Y.; Li, W.; Li, X.; Zhou, P.; Zhuo, W. Slope-Unit Scale Landslide Susceptibility Mapping Based on the Random Forest Model in Deep Valley Areas. *Remote Sens.* **2022**, *14*, 4245. [[CrossRef](#)]
94. Costache, R.; Zaharia, L. Flash-Flood Potential Assessment and Mapping by Integrating the Weights-of-Evidence and Frequency Ratio Statistical Methods in GIS Environment—Case Study: Bâsca Chiojdului River Catchment (Romania). *J. Earth Syst. Sci.* **2017**, *126*, 1–19. [[CrossRef](#)]
95. Zaharia, L.; Costache, R.; Prăvălie, R.; Ioana-Toroimac, G. Mapping Flood and Flooding Potential Indices: A Methodological Approach to Identifying Areas Susceptible to Flood and Flooding Risk. Case Study: The Prahova Catchment (Romania). *Front. Earth Sci.* **2017**, *11*, 229–247. [[CrossRef](#)]
96. Moore, I.D.; Gessler, P.E.; Nielsen, G.A.; Peterson, G.A. Soil Attribute Prediction Using Terrain Analysis. *Soil Sci. Soc. Am. J.* **1993**, *57*, 443–452. [[CrossRef](#)]
97. Pallard, B.; Castellarin, A.; Montanari, A. Hydrology and Earth System Sciences A Look at the Links between Drainage Density and Flood Statistics. *Hydrol. Earth Syst. Sci.* **2009**, *13*, 1019–1029. [[CrossRef](#)]
98. Rennó, C.D.; Nobre, A.D.; Cuartas, L.A.; Soares, J.V.; Hodnett, M.G.; Tomasella, J.; Waterloo, M.J. HAND, a New Terrain Descriptor Using SRTM-DEM: Mapping Terra-Firme Rainforest Environments in Amazonia. *Remote Sens. Environ.* **2008**, *112*, 3469–3481. [[CrossRef](#)]
99. Nobre, A.D.; Cuartas, L.A.; Hodnett, M.; Rennó, C.D.; Rodrigues, G.; Silveira, A.; Waterloo, M.; Saleska, S. Height Above the Nearest Drainage—A Hydrologically Relevant New Terrain Model. *J. Hydrol.* **2011**, *404*, 13–29. [[CrossRef](#)]

100. Rosim, S.; de Freitas Oliveira, J.R.; de Oliveira Ortiz, J.; Cuellar, M.Z.; Jardim, A.C. Drainage Network Extraction of Brazilian Semiarid Region with Potential Flood Indication Areas. In *Proceedings SPIE 9239, Remote Sensing for Agriculture, Ecosystems, and Hydrology XVI*; Neale, C.M.U., Maltese, A., Eds.; SPIE: Amsterdam, The Netherlands, 2014; p. 923919.
101. Rahmati, O.; Kornejady, A.; Samadi, M.; Nobre, A.D.; Melesse, A.M. Development of an Automated GIS Tool for Reproducing the HAND Terrain Model. *Environ. Model. Softw.* **2018**, *102*, 1–12. [[CrossRef](#)]
102. Melton, M.A. The Geomorphic and Paleoclimatic Significance of Alluvial Deposits in Southern Arizona. *J. Geol.* **1965**, *73*, 1–38. [[CrossRef](#)]
103. Conrad, O.; Bechtel, B.; Bock, M.; Dietrich, H.; Fischer, E.; Gerlitz, L.; Wehberg, J.; Wichmann, V.; Böhner, J. System for Automated Geoscientific Analyses (SAGA) v. 2.1.4. *Geosci. Model Dev.* **2015**, *8*, 1991–2007. [[CrossRef](#)]
104. Marchi, L.; Dalla Fontana, G. GIS Morphometric Indicators for the Analysis of Sediment Dynamics in Mountain Basins. *Environ. Geol.* **2005**, *48*, 218–228. [[CrossRef](#)]
105. Moore, I.D.; Wilson, J.P. Length-Slope Factors for the Revised Universal Soil Loss Equation: Simplified Method of Estimation. *J. Soil Water Conserv.* **1992**, *47*, 423–428.
106. Jolliffe, I. Principal Component Analysis. In *Encyclopedia of Statistics in Behavioral Science*; Wiley Online Library: Hoboken, NJ, USA, 2005. [[CrossRef](#)]
107. Carnes, B.A.; Slade, N.A. The Use of Regression for Detecting Competition with Multicollinear Data. *Ecology* **1988**, *69*, 1266–1274. [[CrossRef](#)]
108. Lafi, S.Q.; Kaneene, J.B. An Explanation of the Use of Principal-Components Analysis to Detect and Correct for Multicollinearity. *Prev. Vet. Med.* **1992**, *13*, 261–275. [[CrossRef](#)]
109. Swain, K.C.; Singha, C.; Nayak, L. Flood Susceptibility Mapping through the GIS-AHP Technique Using the Cloud. *ISPRS Int. J. Geo-Inf.* **2020**, *9*, 720. [[CrossRef](#)]
110. Ali, S.A.; Parvin, F.; Pham, Q.B.; Vojtek, M.; Vojteková, J.; Costache, R.; Linh, N.T.T.; Nguyen, H.Q.; Ahmad, A.; Ghorbani, M.A. GIS-Based Comparative Assessment of Flood Susceptibility Mapping Using Hybrid Multi-Criteria Decision-Making Approach, Naïve Bayes Tree, Bivariate Statistics and Logistic Regression: A Case of Topľa Basin, Slovakia. *Ecol. Indic.* **2020**, *117*, 106620. [[CrossRef](#)]
111. Swets, J.A. Measuring the Accuracy of Diagnostic Systems. *Science* **1988**, *240*, 1285–1293. [[CrossRef](#)] [[PubMed](#)]
112. Akbar, T.A.; Hassan, Q.K.; Achari, G. A Methodology for Clustering Lakes in Alberta on the Basis of Water Quality Parameters. *CLEAN Soil Air Water* **2011**, *39*, 916–924. [[CrossRef](#)]
113. Liu, C.W.; Lin, K.H.; Kuo, Y.M. Application of Factor Analysis in the Assessment of Groundwater Quality in a Blackfoot Disease Area in Taiwan. *Sci. Total Environ.* **2003**, *313*, 77–89. [[CrossRef](#)] [[PubMed](#)]
114. Panda, U.C.; Sundaray, S.K.; Rath, P.; Nayak, B.B.; Bhatta, D. Application of Factor and Cluster Analysis for Characterization of River and Estuarine Water Systems—A Case Study: Mahanadi River (India). *J. Hydrol.* **2006**, *331*, 434–445. [[CrossRef](#)]
115. Hazaymeh, K.; Hassan, Q.K. A Remote Sensing-Based Agricultural Drought Indicator and Its Implementation over a Semi-Arid Region, Jordan. *J. Arid Land* **2017**, *9*, 319–330. [[CrossRef](#)]
116. Zhang, C.; Bourque, C.P.A.; Sun, L.; Hassan, Q.K. Spatiotemporal Modeling of Monthly Precipitation in the Upper Shiyang River Watershed in West Central Gansu, Northwest China. *Adv. Atmos. Sci.* **2010**, *27*, 185–194. [[CrossRef](#)]
117. Tehrany, M.S.; Kumar, L.; Neamah Jebur, M.; Shabani, F. Evaluating the Application of the Statistical Index Method in Flood Susceptibility Mapping and Its Comparison with Frequency Ratio and Logistic Regression Methods. *Geomat. Nat. Hazards Risk* **2019**, *10*, 79–101. [[CrossRef](#)]
118. Khosravi, K.; Pourghasemi, H.R.; Chapi, K.; Bahri, M. Flash Flood Susceptibility Analysis and Its Mapping Using Different Bivariate Models in Iran: A Comparison between Shannon’s Entropy, Statistical Index, and Weighting Factor Models. *Environ. Monit. Assess.* **2016**, *188*, 656. [[CrossRef](#)]
119. Mahmoud, S.H.; Gan, T.Y. Multi-Criteria Approach to Develop Flood Susceptibility Maps in Arid Regions of Middle East. *J. Clean. Prod.* **2018**, *196*, 216–229. [[CrossRef](#)]
120. Nsangou, D.; Kpoumié, A.; Mfonka, Z.; Ngouh, A.N.; Fossi, D.H.; Jourdan, C.; Mbele, H.Z.; Mouncherou, O.F.; Vandervaere, J.P.; Ndam Ngoupayou, J.R. Urban Flood Susceptibility Modelling Using AHP and GIS Approach: Case of the Mfoundi Watershed at Yaoundé in the South-Cameroon Plateau. *Sci. Afr.* **2022**, *15*, e01043. [[CrossRef](#)]
121. Bhatt, C.M.; Rao, G.S.; Diwakar, P.G.; Dadhwal, V.K. Development of Flood Inundation Extent Libraries over a Range of Potential Flood Levels: A Practical Framework for Quick Flood Response. *Geomat. Nat. Hazards Risk* **2017**, *8*, 384–401. [[CrossRef](#)]
122. Sharma, V.K.; Rao, G.S.; Bhatt, C.M.; Shukla, A.K.; Mishra, A.K.; Bhanumurthy, V. Automatic Procedures Analyzing Remote Sensing Data to Minimize Flood Response Time: A Step towards National Flood Mapping Service. *Spat. Inf. Res.* **2017**, *25*, 657–663. [[CrossRef](#)]
123. Ishizaka, A.; Labib, A. Analytic Hierarchy Process and Expert Choice: Benefits and Limitations. *OR Insight* **2009**, *22*, 201–220. [[CrossRef](#)]
124. Velasquez, M.; Hester, P.T. An Analysis of Multi-Criteria Decision Making Methods. *Int. J. Oper. Res.* **2013**, *10*, 56–66.
125. Roy, B. Multicriteria Methodology for Decision Aiding. In *Nonconvex Optimization and Its Applications*; Springer US: Boston, MA, USA, 1996; Volume 12, ISBN 978-1-4419-4761-1.

126. Hegger, D.L.T.; Driessen, P.P.J.; Dieperink, C.; Wiering, M.; Raadgever, G.T.T.; van Rijswick, H.F.M.W. Assessing Stability and Dynamics in Flood Risk Governance: An Empirically Illustrated Research Approach. *Water Resour. Manag.* **2014**, *28*, 4127–4142. [[CrossRef](#)]
127. Raadgever, T.; Hegger, D. *Flood Risk Management Strategies and Governance*; Springer: Berlin/Heidelberg, Germany, 2018; ISBN 9783319676982.
128. Driessen, P.P.J.; Hegger, D.L.T.; Kundzewicz, Z.W.; van Rijswick, H.F.M.W.; Crabbé, A.; Larrue, C.; Matczak, P.; Pettersson, M.; Priest, S.; Suykens, C.; et al. Governance Strategies for Improving Flood Resilience in the Face of Climate Change. *Water* **2018**, *10*, 1595. [[CrossRef](#)]
129. Liu, J.; Qi, Y.; Tao, J.; Tao, T. Analysis of the Performance of Machine Learning Models in Predicting the Severity Level of Large-Truck Crashes. *Futur. Transp.* **2022**, *2*, 939–955. [[CrossRef](#)]

Disclaimer/Publisher’s Note: The statements, opinions and data contained in all publications are solely those of the individual author(s) and contributor(s) and not of MDPI and/or the editor(s). MDPI and/or the editor(s) disclaim responsibility for any injury to people or property resulting from any ideas, methods, instructions or products referred to in the content.